

Durham Research Online

Deposited in DRO:

23 August 2018

Version of attached file:

Published Version

Peer-review status of attached file:

Peer-reviewed

Citation for published item:

Ansarinejad, Behzad and Shanks, Tom (2018) 'Detection significance of baryon acoustic oscillations peaks in galaxy and quasar clustering.', *Monthly notices of the Royal Astronomical Society.*, 479 (3). pp. 4091-4107.

Further information on publisher's website:

<https://doi.org/10.1093/mnras/sty1740>

Publisher's copyright statement:

This article has been accepted for publication in *Monthly Notices of the Royal Astronomical Society* ©: 2018
Author(s) Published by Oxford University Press on behalf of the Royal Astronomical Society. All rights reserved.

Additional information:

Use policy

The full-text may be used and/or reproduced, and given to third parties in any format or medium, without prior permission or charge, for personal research or study, educational, or not-for-profit purposes provided that:

- a full bibliographic reference is made to the original source
- a [link](#) is made to the metadata record in DRO
- the full-text is not changed in any way

The full-text must not be sold in any format or medium without the formal permission of the copyright holders.

Please consult the [full DRO policy](#) for further details.



Detection significance of baryon acoustic oscillations peaks in galaxy and quasar clustering

Behzad Ansarinejad[★] and Tom Shanks

Department of Physics, Durham University, South Road, Durham, DH1 3LE, UK

Accepted 2018 June 27. Received 2018 June 27; in original form 2018 February 9

ABSTRACT

We compare our analysis of the baryon acoustic oscillations (BAO) feature in the correlation functions of SDSS BOSS DR12 LOWZ and CMASS galaxy samples with previous literature results. Using subsets of the data we obtain an empirical estimate of the errors on the correlation functions that are in agreement with the simulated errors of previous works. We find that the significance of BAO detection is the quantity most sensitive to the choice of the fitting range with the CMASS value decreasing from 8.0σ to 5.3σ as the fitting range is reduced. Although our measurements of $D_V(z)$ are in agreement with previous studies, we note that their CMASS 8.0σ (LOWZ 4.0σ) detection significance reduces to 4.7σ (2.8σ) in fits with their diagonal covariance terms only. We extend our BAO analysis to higher redshifts by fitting to the weighted mean of 2QDESp, SDSS DR5 UNIFORM, 2QZ, and 2SLAQ quasar correlation functions, obtaining a 7.6 per cent measurement compared to 3.9 per cent achieved by eBOSS DR14. Unlike for the LRG surveys, the larger error on quasar correlation functions implies a smaller role for nuisance parameters (accounting for scale-dependent clustering) in providing a good fit to the fiducial Λ cold dark matter model. Again we find that the eBOSS peak significance reduces from 2.8 to 1.4σ if we ignore the off-diagonal covariance matrix terms in our fitting. We conclude that for both LRGs and quasars, the reported BAO peak significances from the SDSS surveys depend sensitively on the accuracy of the covariance matrix at large separations.

Key words: cosmology: observations – distance scale – large-scale structure of Universe.

1 INTRODUCTION

The determination of the expansion history of the Universe is currently one of the primary goals of observational cosmology. The late-time transition of the expansion rate of the Universe from a deceleration to a phase of acceleration (e.g. based on observational evidence from supernovae; Riess et al. 1998; Perlmutter et al. 1999) in particular, remains one of the most puzzling problems in modern physics. Investigating this problem and exploring the nature of Dark Energy [a hypothetical cause of the accelerated expansion rate of the Universe (Peebles & Ratra 2003), within the framework of Λ cold dark matter (Λ CDM), the current standard cosmological model] have driven efforts to obtain robust and high-precision measurements of the cosmological expansion rate. To this end, a great interest was sparked in exploiting large galaxy redshift surveys in order to constrain the distance-redshift relation across a wide range of redshifts, making use of the baryon acoustic oscillation (BAO) feature in the clustering of galaxies (e.g. Shanks 1985; Blake & Glazebrook 2003; Linder 2003; Seo & Eisenstein 2003; Matsub-

ara 2004; Glazebrook & Blake 2005; Dolney, Jain & Takada 2006; Sánchez, Baugh & Angulo 2008).

A measurement of the BAO signature in the monopole two-point correlation function of the ‘Constant Stellar Mass’ (CMASS) and the low-redshift (LOWZ) galaxy samples from the Data Release 12 (DR12; Alam et al. 2015) of the SDSS BOSS survey was presented by Cuesta et al. (2016). The CMASS and LOWZ samples are extensions to previous SDSS LRG samples.

Here, we first present the results of our independent measurement of the BAO feature in the DR12 CMASS and LOWZ samples. This is followed by a comparison to results of Cuesta et al. (2016) providing an independent verification of the applied methodology, placing particular focus on the uncertainties on the correlation functions. Cuesta et al. (2016) obtained an estimate of the uncertainties based on the covariance matrix of 1000 BOSS DR12 simulated QPM mocks (White, Tinker & McBride 2014). In this study, we divide the data into subsamples upon which measurements of the correlation function are performed, giving an empirical estimate of the uncertainty on the mean correlation function. Furthermore, we investigate certain aspects of the fitting procedure commonly implemented in BAO analysis studies. These include the extent of the role played by the nuisance fitting parameters in providing a

[★] E-mail: behzad.ansarinejad@durham.ac.uk

good fit; effects of the choice of the fitting range on the results and a comparison between fits using the full BOSS DR12 QPM covariance matrices and their diagonal elements only. Here, our main goal is to investigate the robustness of the BAO peak detection significance to variations in different aspects of the fitting procedure. Note that in this work we do not attempt to perform reconstruction and hence we simply draw comparison with the pre-reconstruction results throughout.

At higher redshifts, BAO have also been detected in the Lyman-alpha forest in the BOSS quasar survey at $2.1 < z < 3.3$ (Slosar et al. 2013; Delubac et al. 2015). As originally suggested by Sawangwit et al. (2012), it is also possible to make accurate BAO measurements in the $z < 2.2$ range using quasars as direct tracers of the matter distribution. The eBOSS survey (Dawson et al. 2016) is therefore making BAO measurements via quasars using them both directly as tracers and via the Lyman-alpha forest. Here, we shall use the SDSS DR5 (Ross et al. 2009), 2SLAQ (Croom et al. 2009), 2QZ (Croom et al. 2004), and 2QDES pilot (Chehade et al. 2016) surveys to determine the level of accuracy to which the BAO scale can be measured by the previous generation of quasar surveys used as direct tracers in the $0.8 < z < 2.2$ redshift range. Furthermore, we combine our results with those of Ata et al. (2018), who performed BAO analysis on the eBOSS DR14 quasar sample in the same redshift range, obtaining a BAO distance measurement based on the combination of these samples.

The layout of this paper is as follows: Section 2 contains a brief description of the galaxy samples along with the basic properties of the selected subsamples. In Section 3, we present a description of the relevant methodology involved in measuring the correlation function, error analysis, and the fitting procedure. This is followed by a presentation and discussion of our results and a comparison of our findings with those of Cuesta et al. (2016) in Section 4. In Section 5, we provide a description of the quasar samples used in our high redshift BAO analysis, followed by an outline of our applied methodology in Section 6. We present the results of our QSO BAO analysis in Section 7, along with the cosmological distance constraints obtained from our QSO and LRG measurements, comparing our findings with the predictions of Planck Collaboration (2016). Finally, we conclude this work by providing a summary of our findings in Section 8.

2 DATA SETS

In this study, we first use a set of 777 202 galaxies in the redshift range $0.43 < z < 0.7$ from the BOSS DR12 CMASS sample, with an effective redshift of 0.57, and 361 762 galaxies in the redshift range $0.15 < z < 0.43$ from the DR12 LOWZ sample, with an effective redshift of 0.32. The CMASS and LOWZ samples have been limited to magnitudes of $17.5 < i_{\text{cmid}} < 19.9$ and $16 < r_{\text{cmid}} < 19.6$, respectively. Full details of the target selection criteria can be found in Reid et al. (2016) and the treatment of systematics and the relevant corrections is discussed in Ross et al. (2017). In accordance with Cuesta et al. (2016), the samples, mocks, and random data sets were obtained from the DR12 data base.¹ The redshift distributions $n(z)$ of the galaxies in the DR12 CMASS and LOWZ samples are displayed in Fig. 1.

In order to obtain an empirical estimate of the uncertainties on the correlation functions, the CMASS sample is subsetted into five fields (subsamples) of equal size covering an overall area of

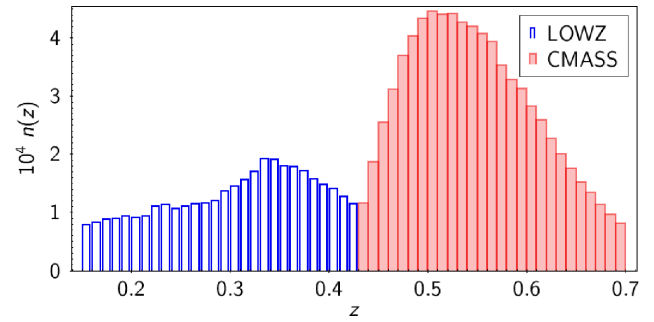


Figure 1. The redshift distribution of the BOSS DR12 LOWZ and CMASS samples analysed in this study, as well as in Cuesta et al. (2016). Bins are $\Delta z = 0.01$ in width.

8487.77 deg^2 , about 90.5 percent of the total effective sample area (9376.09 deg^2). The LOWZ sample is similarly divided into five equally sized fields covering 7294.87 deg^2 , roughly 87.5 percent of the total sample area (8337.47 deg^2). Initially, dividing the samples into five fields was deemed sufficient in order to produce an estimate of the uncertainties to a reasonable degree of accuracy. However, as demonstrated in later sections, the precision of the empirical estimate of uncertainties can be further improved by using a larger number of subsamples. The positions of all selected fields are illustrated in Fig. 2, with Table 1 providing a description of the basic properties of the selected fields. Once the correlation function for each field is obtained, a mean correlation function is calculated and is taken to represent the correlation function of the sample, using the standard error on the mean as an estimate of the uncertainty.

In our analysis up to Section 5, we assume the same fiducial cosmology as Cuesta et al. (2016) with $\Omega_m = 0.29$, $\Omega_b h^2 = 0.02247$, $\Omega_\Lambda = 0.71$, $\Omega_k = 0$, $\Omega_v = 0$, $h = 0.7$, $w = -1$, $n_s = 0.97$ and $\sigma_8 = 0.8$. The fiducial distances to $z = 0.32$ and 0.57 (the effective redshifts of our samples) based on our assumed cosmology are presented in Table 2.

3 METHODOLOGY

3.1 Measuring the correlation function

The monopole two-point correlation function (in redshift-space), $\xi(s)$, is calculated for each individual field using the CUTE² algorithm described by Alonso (2012).

To perform the measurement of the correlation function, we make use of the Landy-Szalay estimator (Landy & Szalay 1993),

$$\xi(s) = \frac{DD(s) - 2DR(s) + RR(s)}{RR(s)}, \quad (1)$$

where $DD(s)$, $DR(s)$, and $RR(s)$ are data-data, data-random, and random-random pair-counts, respectively.

In our analysis, we make use of the BOSS DR12 FKP-weighted (Feldman, Kaiser & Peacock 1994) randoms, and in accordance with Reid et al. (2016), apply a weighting of $w_{\text{tot}} w_{\text{FKP}}$ to the galaxies. A full description of the constituents of w_{tot} is presented in Reid et al. (2016); in short, this weight consists of three terms which account for effects of angular systematics, fibre collisions, and redshift failures. In order to facilitate direct comparison with the findings of Cuesta et al. (2016), we sum our pair counts into 25 bins of width

¹<https://data.sdss.org/sas/dr12/boos/lss/>

²<http://members.ift.uam-csic.es/dmonge/CUTE.html>

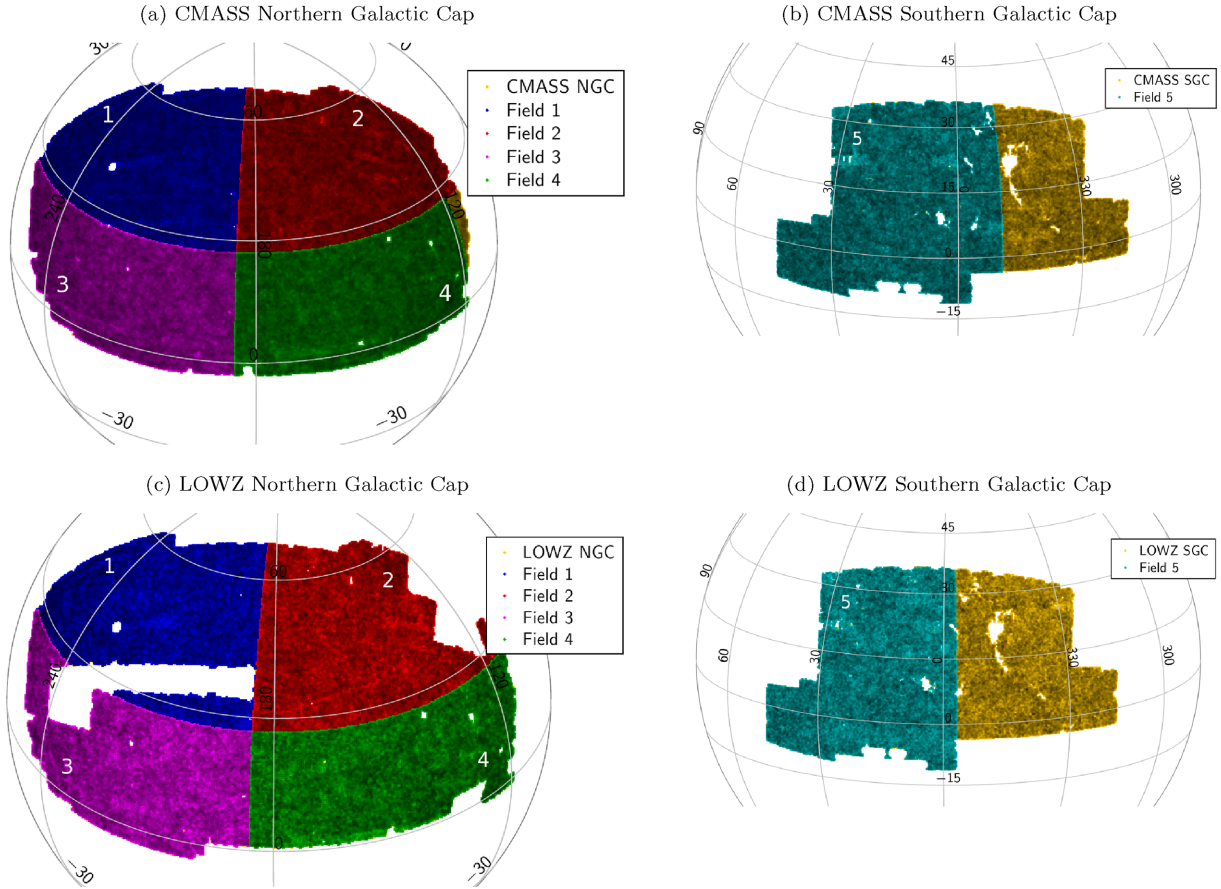


Figure 2. The coverage of the five selected fields in the Northern and Southern Galactic caps of the CMASS and LOWZ samples. The sample areas not selected are shown in yellow. The basic properties of these fields can be found in Table 1.

Table 1. The basic properties of the five chosen fields (shown in Fig. 2) in the CMASS and LOWZ samples.

CMASS				
Field	Ra°	Dec°	Area (deg ²)	Number of galaxies
1	>185	>27	1703	142 636
2	<185	>27	1686	141 706
3	>185	<27	1699	141 847
4	119–185	<27	1698	137 891
5	350–45.5	>–11	1701	144 820
LOWZ				
Field	Ra°	Dec°	Area (deg ²)	Number of galaxies
1	>185	>27	1447	61 319
2	<185	>27	1453	63 109
3	>185	<27	1474	61 605
4	<185	<27	1463	63 431
5	357–45.5	>–11	1459	68 057

$8 h^{-1}$ Mpc in our calculation of the correlation functions, covering the range of $s \leq 200 h^{-1}$ Mpc in redshift space.

3.2 Error analysis

Following the procedure proposed by Norberg et al. (2009), the bootstrap resampling method is used to provide an estimate of the errors on the mean correlation functions of our CMASS and

LOWZ samples. In total, we generate $N = 100$ resamplings and obtain the mean correlation function $\bar{\xi}(s)$ of these resamplings. As demonstrated by Norberg et al. (2009), an oversampling factor of 3 appears to be optimal in improving the bootstrap recipe. Hence, we calculate the mean correlation function of each resampling, ξ_n , based on the correlation functions of $N_r = 3 \times N_{\text{sub}}$ randomly selected subvolumes (with replacement), from the original $N_{\text{sub}} = 5$ subvolumes defined in Section 2 for the CMASS and LOWZ samples.

A second set of errors are determined for the mean correlation functions of our samples, simply based on obtaining the standard errors on the mean. This is done using

$$\sigma_{\text{mean}} = \frac{\sigma_{N_{\text{sub}}-1}}{\sqrt{N_{\text{sub}}}} = \sqrt{\frac{\sum (\xi_i - \bar{\xi})^2}{N_{\text{sub}}^2 - N_{\text{sub}}}}, \quad (2)$$

where $\sigma_{N_{\text{sub}}-1}$ is the standard deviation normalized to $N_{\text{sub}} - 1$ (as σ_{mean} is obtained from the same data set reducing the number of degrees of freedom by one); N_{sub} is the number of subvolumes in each sample (i.e. 5); ξ_i is the correlation function of the i th subvolume, and $\bar{\xi}$ is the mean correlation function of the sample.

A comparison of the estimated errors from these two different methods and the errors found by Cuesta et al. (2016) based on the covariance matrix of the DR12 QPM mocks is presented in Section 4.2.

Table 2. A summary of the fiducial distances and values of the Hubble parameter used in this work and by Cuesta et al. (2016), computed at the effective redshifts of the LOWZ ($z = 0.32$) and CMASS ($z = 0.57$) samples, based on our assumed flat Λ CDM cosmological model.

r_d (Mpc)	$D_A(z = 0.32)$ (Mpc)	$H(z = 0.32)$ (km s ⁻¹ Mpc ⁻¹)	$D_V(z = 0.32)$ (Mpc)	$D_A(z = 0.57)$ (Mpc)	$H(z = 0.57)$ (km s ⁻¹ Mpc ⁻¹)	$D_V(z = 0.57)$ (Mpc)
147.10	962.43	82.142	1235.28	1351.13	94.753	2009.55

3.3 Fitting the correlation function

To fit the correlation functions, we follow a procedure based on the methods described in Xu et al. (2012) and Anderson et al. (2012). We present a brief description of these techniques in this section.

We use a fitting model of the form

$$\xi^{\text{fit}}(s) = B^2 \xi_m(\alpha s) + A(s), \quad (3)$$

where ξ_m is defined in equation (7), B^2 is a constant term allowing for any unknown large-scale bias, and $A(s)$ is given by

$$A(s) = \frac{a_1}{s^2} + \frac{a_2}{s} + a_3, \quad (4)$$

where $a_{1,2,3}$ are nuisance parameters. The $A(s)$ term is included in order to marginalize over broad-band effects due to redshift-space distortions and scale-dependent bias as well as any errors made in our assumption of the fiducial cosmology. The form of the $A(s)$ term was chosen by Xu et al. (2012) due to its simplicity and was further justified in that work by comparing it to various alternatives and demonstrating that it performs optimally in providing a good fit. We can obtain distance constraints by finding the optimum value of the scale dilation parameter α . This parameter provides a measure of any isotropic shifts in the position of the BAO peak in the data compared to the fiducial model, due to non-linear structure growth. This term is defined as

$$\alpha = \frac{D_V(z)}{r_d} \frac{r_{d,\text{fid}}}{D_{V,\text{fid}}(z)}, \quad (5)$$

where z is the redshift, r_d is the sound horizon at the drag epoch, and fid denotes the fiducial values (given in Table 2). An $\alpha > 1$ ($\alpha < 1$) indicates that the BAO peak in the observed data is located at a smaller (larger) scale compared to the peak in the model. The approximate volume-averaged distance to redshift z is

$$D_V(z) \equiv \left[cz(1+z)^2 \frac{D_A(z)^2}{H(z)} \right]^{1/3}, \quad (6)$$

where $D_A(z)$ is the angular diameter distance and $H(z)$ is the Hubble parameter at redshift z . This ‘distance’ is proportional to the volume-averaged dilation factors (Ballinger, Peacock & Heavens 1996) in the redshift and angular directions at a redshift z .

The model correlation function in equation (3), ξ_m , is given by

$$\xi_m(s) = \int \frac{k^2 dk}{2\pi^2} P_m(k) j_0(ks) e^{-k^2 a^2}, \quad (7)$$

where the Gaussian term is added to damp the oscillatory transform kernel $j_0(ks) = \sin(ks)/ks$ at high- k . Here, we set $a = 2 \text{ h}^{-1} \text{ Mpc}$, which is small enough as to not cause significant damping effects at our scales of interest.

The template power spectrum is given by

$$P_m(k) = [P_{\text{lin}}(k) - P_{\text{noBAO}}(k)] e^{-k^2 \sum_{\text{nl}}^2 / 2} + P_{\text{noBAO}}(k), \quad (8)$$

where P_{lin} is the linear power spectrum at $z = 0$ (generated using CAMB;³ Lewis, Challinor & Lasenby 2000) and P_{noBAO} is the power

spectrum with the BAO feature removed as described in Eisenstein & Hu (1998). The $\sum_{\text{nl}}^2 / 2$ term damps the BAO features in P_{lin} , accounting for the effects of non-linear structure evolution. Here, we set $\sum_{\text{nl}} = 8 \text{ h}^{-1} \text{ Mpc}$.

The best-fitting values of the B^2 , a_1 , a_2 , and a_3 fitting parameters in equation (3) are determined using the `scipy.optimize.curve_fit` module in PYTHON, which makes use of the Levenberg–Marquardt algorithm. To obtain the optimum value of α we compute the χ^2 goodness-of-fit indicator for fits obtained from shifting the model in the range $0.8 < \alpha < 1.2$ with intervals of $\Delta\alpha = 0.0001$, taking the value of α which corresponds to the minimum χ^2 , (χ_{min}^2).

The χ^2 function is given by

$$\chi^2(\alpha) = [\xi^{\text{obs}} - \xi^{\text{fit}}(\alpha)]^T C^{-1} [\xi^{\text{obs}} - \xi^{\text{fit}}(\alpha)], \quad (9)$$

where ξ^{obs} is the observed correlation function, $\xi^{\text{fit}}(\alpha)$ is the best-fitting model at each α , and C is the BOSS DR12 covariance matrix obtained from 1000 simulated QPM mocks.

In this study, we investigate potential effects on the measured value of α and its uncertainty based on fitting the data across various ranges, using the complete ξ^{fit} model with and without the $A(s)$ nuisance parameters. Furthermore, by comparing the $\Delta\chi^2$ versus α curves from fitting the ξ^{fit} and ξ^{noBAO} models (the latter is obtained by setting the term $P_m = P_{\text{noBAO}}$ in the model correlation function ξ_m), we obtain a measure of the significance at which the BAO signature is detected in the data. Here, $\Delta\chi^2 = \chi^2(\alpha) - \chi_{\text{min}}^2$.

To obtain an estimate of the uncertainty in α , we assume a Gaussian form for the probability distribution of α

$$p(\alpha_i) = \frac{e^{-\chi^2(\alpha_i)/2}}{\sum_j e^{-\chi^2(\alpha_j)/2} \Delta\alpha}, \quad (10)$$

where the denominator is a normalization factor ensuring the distribution integrates to unity. In effect, $p(\alpha_i)$ is the probability that the acoustic scale $\alpha = \alpha_i$, based on the χ^2 distribution obtained from comparing the model ξ^{fit} [equation (3) with α_i], to our observed correlation function ξ^{obs} . We then calculate the standard deviation of our probability distribution which serves as an estimate of the uncertainty in α :

$$\sigma_\alpha = \sqrt{\langle \alpha^2 \rangle - \langle \alpha \rangle^2}, \quad (11)$$

here, $\langle \alpha \rangle$ represents the mean of the $p(\alpha_i)$ distribution given by

$$\langle \alpha \rangle = \sum_i \alpha_i p(\alpha_i) \Delta\alpha, \quad (12)$$

and

$$\langle \alpha^2 \rangle = \sum_i \alpha_i^2 p(\alpha_i) \Delta\alpha. \quad (13)$$

The estimated uncertainty obtained from this method is equivalent to the value given by the $\Delta\chi^2$ curve at the 1σ level.

4 RESULTS AND DISCUSSION

The correlation functions of the individual fields for the LOWZ and CMASS samples along with the corresponding mean correlation

³<http://cosmologist.info/camb/>

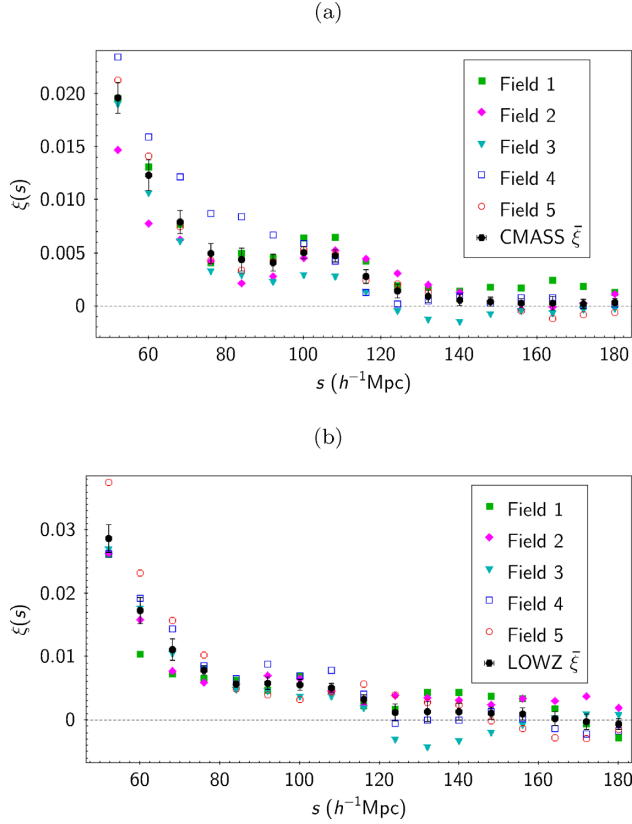


Figure 3. The monopole correlation functions for the individual fields (1, filled squares; 2, filled diamonds; 3, filled triangles; 4, open squares; 5, open circles) and the corresponding mean correlation function (black filled circles), of (a) CMASS and (b) LOWZ samples. The error bars on the mean correlation functions are the standard error on the mean.

functions are displayed in Fig. 3. We note that there is quite a wide variation in these correlation functions with e.g. field 4 for CMASS showing high values at $\sim 80 h^{-1}\text{Mpc}$. In the following sections, we compare our measurement of the mean correlation functions with the measurements of Cuesta et al. (2016), perform fitting to the mean correlation functions and analyse various aspects of the fitting procedure. Furthermore, we obtain measurements of $D_V(z)$ based on our measured position of the BAO peak.

4.1 Comparison with Cuesta et al. (2016)

Fig. 4 shows a comparison between our mean correlation functions and the correlation functions obtained by Cuesta et al. (2016) for the DR12 LOWZ and CMASS samples. We find that our measured correlation functions are in excellent agreement with those presented in Cuesta et al. (2016), and we observe no significant changes when we replace the BOSS DR12 randoms with randoms generated by CUTE. Furthermore, we observe no significant variations when we do not apply any weights to the data or randoms. This outcome is however expected due to the high completeness of 98.8 per cent and 97.2 per cent for the CMASS and LOWZ samples, respectively (see fig. 8 of Reid et al. 2016).

4.2 Error analysis results

This section contains a comparison between our two measures of uncertainties (standard error and bootstrap resampling) on the mean

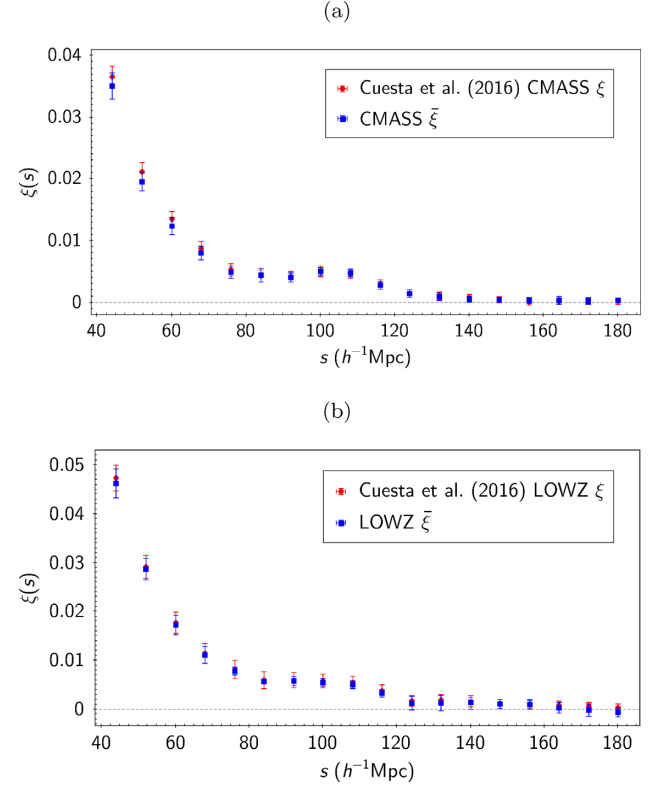


Figure 4. A comparison of our mean monopole correlation functions (blue squares) for (a) DR12 CMASS and (b) LOWZ samples, and the pre-reconstruction correlation functions presented in Fig. 1 of Cuesta et al. (2016) (red circles) for these samples. Error bars on our measurements represent the standard error on the mean based on our five subsamples, while the error bars on the Cuesta et al. (2016) data points are based on the BOSS DR12 covariance matrix, obtained from simulated mocks.

correlation functions of the LOWZ and CMASS samples. Here, we also include the bootstrap uncertainties based on dividing the CMASS sample into 30 subsamples (see figures in Appendix A). We distinguish between the two bootstrap uncertainties using the labels ‘CMASS 5’ and ‘CMASS 30’. More importantly comparisons are drawn between our measured empirical errors and errors obtained from simulations presented in Cuesta et al. (2016) for the correlation functions of the LOWZ and CMASS samples. In order to account for the fact that our selected fields do not cover the entire sample area, when comparing our results with those from Cuesta et al. (2016) we scale our measured errors by the square root of the ratio of the total coverage area of our fields to the total sample area.

As shown in Figs 5(a) and (b), we find a good agreement between the standard error and bootstrap error estimates for both samples. Fig. 5(a) shows that at our main scale of interest (in the vicinity of the $108 h^{-1}\text{Mpc}$ bin where the BAO peak lies), our results for the five fields CMASS sample also appear to be in reasonable agreement with the errors presented by Cuesta et al. (2016). Furthermore, our 30 fields bootstrap uncertainties appear to be in excellent agreement with those from Cuesta et al. (2016) at scales larger than $90 h^{-1}\text{Mpc}$. To provide a quantitative demonstration of the level agreement between the errors from Cuesta et al. (2016) and the simple case of standard errors obtained from five fields, we make use of the fractional error in the error, given by $1/\sqrt{2N-2}$ (Squires 2001). Here, N is the number of measurements (in our case

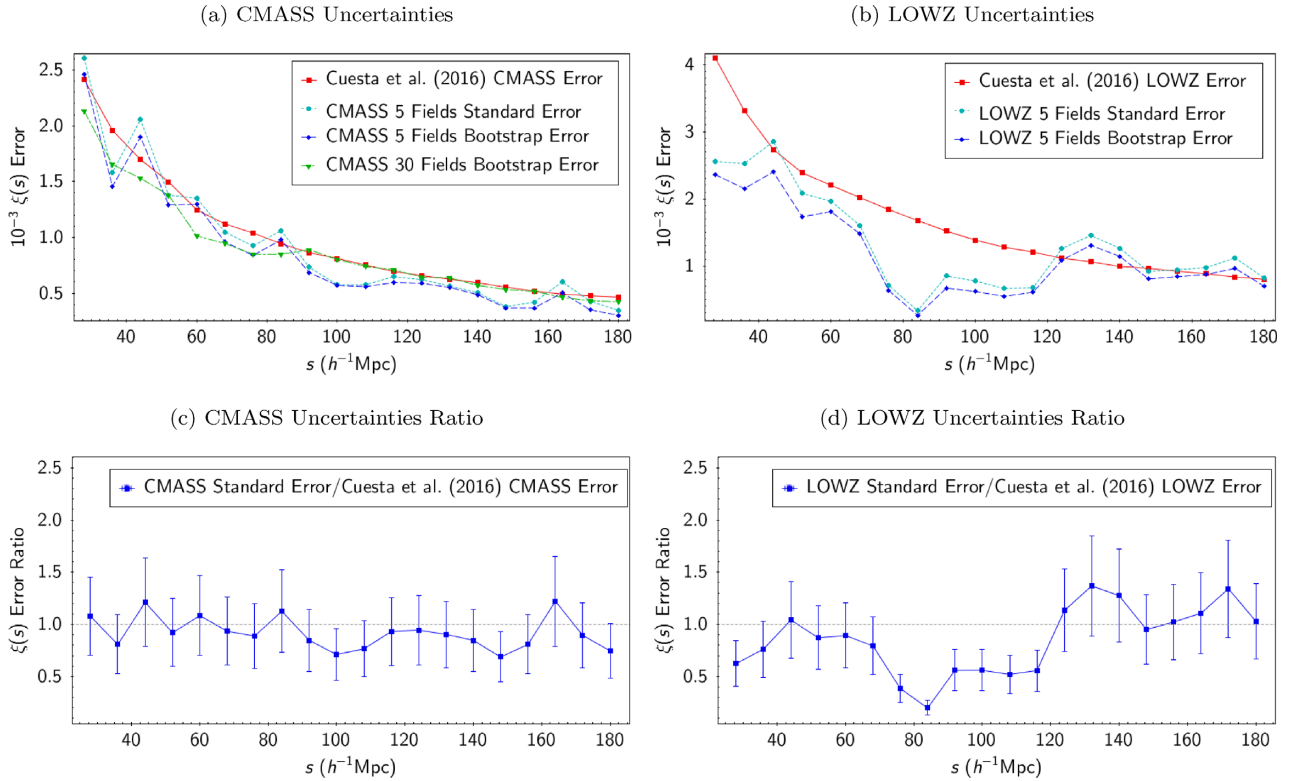


Figure 5. A comparison of the uncertainties on our measured mean correlation function of the CMASS sample, at our primary fitting range $28 \leq s \leq 180 h^{-1} \text{Mpc}$. The standard error on the mean (light blue circles) and bootstrap (dark blue diamonds) estimates of error for the five fields appear to be in good agreement. The bootstrap error from the 30 fields (green inverted triangles) and the uncertainties on the measured correlation functions of Cuesta et al. (2016) (Fig. 1; red squares) are also plotted, showing excellent agreement between the two at scales larger than $90 h^{-1} \text{Mpc}$. Here, all our measured errors are scaled by the square root of the ratio of the area covered by our selected fields, to the total sample area (e.g. in the case of five fields CMASS by $\sqrt{0.905}$). Subplot (c) shows the ratio of our standard error to the errors presented by Cuesta et al. (2016) for the CMASS sample. Here, the error bars represent the error in the error (see the discussion in Section 4.2). Subplots (b) and (d) contain the equivalent results for the LOWZ sample.

5), giving a fractional error in the error of ≈ 35 percent. Fig. 5(c) shows the ratio of our measured standard error to the errors presented by Cuesta et al. (2016) for the CMASS sample with the error bars being the error on our measured standard error. We can see that at the $108 h^{-1} \text{Mpc}$ bin this ratio is 0.8 which is consistent with unity within the error bars, and the general agreement between the errors is an indication that the QPM mocks reproduce an accurate representation of the data. As shown in Fig. 5(d) however, in the case of the LOWZ sample the ratio between the two errors varies to a greater extent as a function of scale, with the discrepancy between the two errors being larger around the BAO scale. This indicates that the errors presented by Cuesta et al. (2016) do not appear to be underestimated in this region.

4.3 Data-fitting results

The best-fitting values of α obtained from fitting the data with various models, across 20 bins, with centres in the range $28 \leq s \leq 180 h^{-1} \text{Mpc}$ are summarised in Table 3.⁴ The pre-reconstruction

best-fitting values of α from Cuesta et al. (2016) are included in this table for comparison. Here, ‘ α ’ refers to values obtained from fitting to the mean correlation functions of the LOWZ and CMASS samples, with errors given by the procedure described in Section 3.3. The ‘5-fields $\bar{\alpha}$ ’ values in this table are obtained by fitting to the correlation functions of each field individually resulting in five measurements of α (these are presented in Table 4), and calculating the mean and standard error of these measurements. When fitting to correlation functions of individual fields we scale the BOSS DR12 covariance matrix by a factor of 5.

As shown in Table 3, we find that our measured ‘5-fields $\bar{\alpha}$ ’ values are in good agreement with our overall values of α . This demonstrates the robustness of the implemented fitting procedure in producing an accurate measurement of the position of the BAO peak. Furthermore, when comparing the results corresponding to fits with the complete model, we find that for both CMASS and LOWZ samples, our measured values of α are in agreement with the measurement presented by Cuesta et al. (2016), with the errors on α being similar in size.

We find the values of α measured for the individual fields in Table 4 to be in general agreement with the measurements of α from Cuesta et al. 2016. In cases where there appears to be a divergence between the measurements, (for instance our result of fitting the correlation function of field 4 in the CMASS sample with the complete model appears to be $\approx 1.7\sigma$ away from the value of α measured by Cuesta et al. 2016), the dependency seems to be due

⁴Note that we place the main focus of our analysis on the results corresponding to this fitting range in order to match the fitting range chosen in Cuesta et al. (2016), allowing for direct comparison of the results. As discussed in Section 3.3, when fitting the correlation functions we use the BOSS DR12 covariance matrix used in the analysis of Cuesta et al. (2016).

Table 3. Results of fitting the correlation functions of the LOWZ and CMASS samples using the complete ξ^{fit} model described in equation (3) and the same model without the $A(s)$ nuisance fitting parameters. In line with Cuesta et al. (2016) the fitting is performed in the range $28 \leq s \leq 180 h^{-1} \text{ Mpc}$. Here, the ‘ α ’ values are obtained from fitting to the mean correlation function $\bar{\xi}(s)$ of each sample, presenting the corresponding χ^2_{min} over the number of degrees of freedom and ‘Significance’ refers to the significance of the detection of the BAO peak, using the complete fitting model (see Section 4.5). The F -ratio p -values (given by equation 14) indicate the probability that the nuisance parameters do not contribute to the goodness-of-fit of the full model. The ‘5-fields $\bar{\alpha}$ ’ values are based on taking the mean and standard error of the individual α s, measured from fits to correlation functions of the five fields in the LOWZ and CMASS samples (see Table 4). We have used the BOSS DR12 covariance matrices in our fits scaling them by a factor of 5 when fitting to the five fields individually. For comparison, the best-fitting values of α from Cuesta et al. (2016) (Table 10), for the pre-reconstruction LOWZ and CMASS sample are also included.

This work	Model	α	$\chi^2_{\text{min}}/\text{dof}$	Significance	F -ratio	5-fields $\bar{\alpha}$
CMASS	$B^2\xi_m + A(s)$	1.0109 ± 0.0121	14.9/15	8.0σ	$4.56 (p = 0.018)$	1.0122 ± 0.0172
	$B^2\xi_m$	1.0009 ± 0.0116	28.5/18	6.9σ		1.0021 ± 0.0101
LOWZ	$B^2\xi_m + A(s)$	1.0074 ± 0.0266	15.5/15	4.3σ	$9.68 (p = 0.00084)$	1.0050 ± 0.0421
	$B^2\xi_m$	0.9698 ± 0.0523	45.5/18	1.8σ		1.0060 ± 0.0195
Cuesta et al. (2016)	Model	α	$\chi^2_{\text{min}}/\text{dof}$	Significance		
CMASS	$B^2\xi_m + A(s)$	1.0153 ± 0.0134	12/15	8.0σ		
LOWZ	$B^2\xi_m + A(s)$	1.0085 ± 0.0300	13/15	4.0σ		

Table 4. Results of fitting the correlation functions of the five individual fields in the LOWZ and CMASS samples using two different models, over the range $28 \leq s \leq 180 h^{-1} \text{ Mpc}$. Here, we have used the BOSS DR12 covariance matrices, scaled by a factor of 5 and ‘Significance’ refers to the significance of the detection of the BAO peak, using the complete fitting model (see Section 4.5). The mean α and its standard error obtained based on the values of α in this table are presented under the ‘5-fields $\bar{\alpha}$ ’ column in Table 3.

This work	Field	Model	α	$\chi^2_{\text{min}}/\text{dof}$	Significance
CMASS	1	$B^2\xi_m + A(s)$	1.0070 ± 0.0207	14.5/15	4.2σ
		$B^2\xi_m$	1.0034 ± 0.0219	21.7/18	
	2	$B^2\xi_m + A(s)$	0.9656 ± 0.0245	16.2/15	3.3σ
		$B^2\xi_m$	0.9751 ± 0.0279	21.1/18	
	3	$B^2\xi_m + A(s)$	0.9924 ± 0.0406	12.6/15	2.9σ
		$B^2\xi_m$	0.9848 ± 0.0273	12.2/18	
	4	$B^2\xi_m + A(s)$	1.0703 ± 0.0506	13.5/15	2.0σ
		$B^2\xi_m$	1.0273 ± 0.0380	29.7/18	
	5	$B^2\xi_m + A(s)$	1.0319 ± 0.0258	10.8/15	3.3σ
		$B^2\xi_m$	1.0221 ± 0.0261	12.2/18	
LOWZ	1	$B^2\xi_m + A(s)$	1.0535 ± 0.0703	34.6/15	1.3σ
		$B^2\xi_m$	1.0403 ± 0.0711	35.3/18	
	2	$B^2\xi_m + A(s)$	1.1049 ± 0.1159	23.7/15	1.6σ
		$B^2\xi_m$	1.0624 ± 0.0290	33.8/18	
	3	$B^2\xi_m + A(s)$	1.0117 ± 0.0765	17.0/15	1.8σ
		$B^2\xi_m$	0.9817 ± 0.0344	16.3/18	
	4	$B^2\xi_m + A(s)$	1.0210 ± 0.0361	22.3/15	2.3σ
		$B^2\xi_m$	1.0009 ± 0.0363	26.0/18	
	5	$B^2\xi_m + A(s)$	0.8674 ± 0.0934	18.2/15	1.7σ
		$B^2\xi_m$	0.9527 ± 0.0125	43.5/18	

to the shape of the BAO peak (which in this case appears to be relatively flat, as seen in Fig. 3a). However, as the ‘5-fields $\bar{\alpha}$ ’ values are in agreement with the measurements of α from the mean correlation functions, these effects seem to cancel out when we take the average over the 5 fields, even given our relatively small number of subsamples.

The performance of the two models in fitting the correlation functions (given by the $\chi^2_{\text{min}}/\text{dof}$ goodness-of-fit indicator) also appear to vary largely depending on the shape of the correlation function. However, with the exception of certain fields (for instance field 3 of both CMASS and LOWZ samples), the complete model appears to perform better overall in providing good fits. It is important to note however that the performance of a model in providing a good fit is not necessarily indicative that the correlation function has provided a representative and accurate measurement of α , and one should also consider the shape and prominence of the BAO peak in the corre-

lation function itself.⁵ This is exemplified by field 4 in the CMASS sample where the $\chi^2_{\text{min}}/\text{dof}$ value indicates that the complete model has provided a reasonably good fit to the data but due to the shape of the correlation function (see Fig. 3a), an accurate determination of the position of the peak has not been possible. Finally, we find that the significance of detection of the peak in the individual fields to be generally lower than the significance of the detection of the peaks in the mean correlation functions of the two samples (as shown in Table 3). This is a further indication of the lack of prominent and well-defined peaks in the correlation functions of the individual fields and as shown once again by field 4 in the CMASS sample,

⁵In Section 4.5, we discuss how the shape of the $\Delta\chi^2$ curve could also provide a measure of the degree to which we could be confident in our measurement of α .

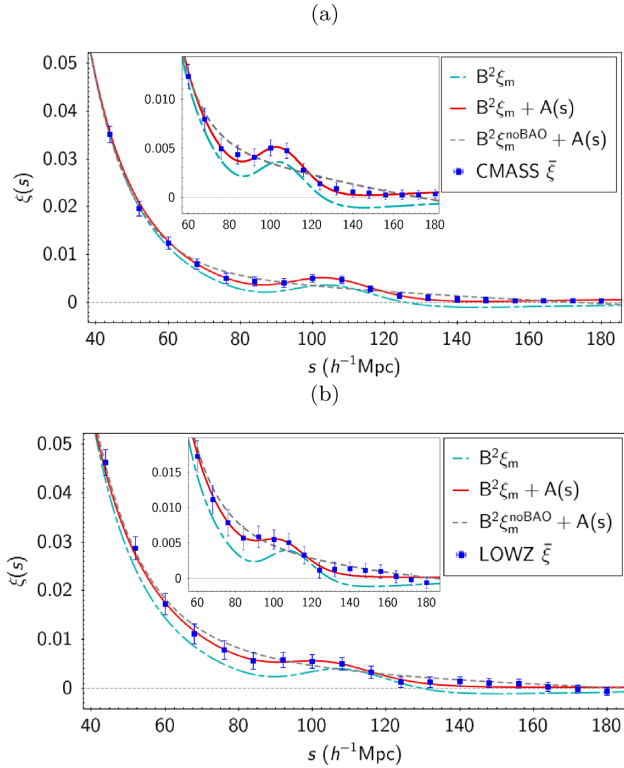


Figure 6. The results of fitting the mean correlation function of (a) CMASS and (b) LOWZ samples with various fitting models in the range $28 \leq s \leq 180 h^{-1} \text{ Mpc}$. The blue dot-dashed curve is the ξ^{fit} model (equation 3) with the B fitting parameter only, while the red solid curve shows the same model fitted with both B and $A(s)$ fitting terms. The grey dashed curve is the ξ^{noBAO} model fitted with the B and $A(s)$ fitting terms. The error bars shown are the square root of the diagonal elements of the BOSS DR12 covariance matrices.

a low significance of detection of the peak could also hint towards the potential unreliability of the measured α .

4.4 Model comparison

Fig. 6 shows the results of fitting the mean correlation functions of the CMASS and LOWZ samples with the ξ^{fit} model, fitted with and without the $A(s)$ nuisance parameters, and the ξ^{noBAO} model fitted with both B and $A(s)$ fitting terms. The important role played by the $A(s)$ nuisance fitting terms in producing a good fit is highlighted in these plots. This is also demonstrated numerically in Table 3, with the fits without the $A(s)$ having increased $\chi^2_{\text{min}}/\text{dof}$ values indicating the lower quality of fits. We assess the $\chi^2_{\text{min}}/\text{dof}$ statistic based on the corresponding p -value $= 1 - p(\chi^2(\text{dof}) \geq \chi^2_{\text{min}} | H)$, which is defined as the probability of obtaining a $\chi^2(\text{dof})$ value at least as extreme as the value obtained, given our null hypothesis H : that the data are consistent with the model. In other words, the p -value is the probability of obtaining the observed data, under the assumption that the model is correct, and a measure of the significance at which the model is rejected by the data is given by $1 - p$ -value.

We note that the visual impression given in Fig. 5(a) is that the ΛCDM model without nuisance parameters for the CMASS sample is rejected at a higher significance than by the $28.5/18$ ($p = 0.055$) indicated in Table 3. Indeed, when only the diagonal terms of the covariance matrix are used in the fitting, the significance of rejection rises to $64.9/18$ ($p = 3.23 \times 10^{-7}$) (see Table 5). Thus, in this case

the inclusion of the full covariance matrix causes a large reduction in $\chi^2_{\text{min}}/\text{dof}$.

We then take a more detailed look at how significant the nuisance parameters are in achieving a good fit for the ΛCDM model. Given our two nested fit models, we can make use of the F -ratio (see e.g. Gregory 2005) in order to determine whether the use of the more complex model results in a statistically significant improvement in fit quality. The F -ratio is given by

$$F = \frac{(\chi^2_{\text{simple}} - \chi^2_{\text{complex}})/(\text{dof}_{\text{simple}} - \text{dof}_{\text{complex}})}{\chi^2_{\text{complex}}/\text{dof}_{\text{complex}}}. \quad (14)$$

Here, χ^2_{simple} and χ^2_{complex} refer to the χ^2_{min} values obtained from fitting the ξ^{fit} model without the $A(s)$ nuisance fitting terms, and by the complete ξ^{fit} model, respectively, and dof are the degrees of freedom associated with each model. Once the F value is obtained we can test the validity of our null hypothesis that the complex model does not provide a significantly better fit than the simple model. Similar to the χ^2 analysis above, we assess the validity of the null hypothesis based on the p -value associated with the resulting F statistic.

Based on the $\chi^2_{\text{min}}/\text{dof}$ values presented in Table 3, for the fitting range $28 \leq s \leq 180 h^{-1} \text{ Mpc}$, we obtain F -values of 4.56 ($p = 0.018$) and 9.68 ($p = 0.00084$) for the CMASS and LOWZ samples, respectively. In other words our simple model is rejected in favour of the full ξ^{fit} model by the data (given that assuming the null hypothesis is correct, i.e. that there is no significant difference between the two models, the probability of obtaining an F statistic at least as extreme as the values here by chance are ≈ 1.8 per cent and 0.1 per cent for the CMASS and LOWZ samples, respectively). This means that the inclusion of the nuisance parameters results in a significant improvement to the fit. This is specially true in the case of the LOWZ sample, where as seen in Fig. 5(b), the BAO peak in the correlation function appears flatter in the ≈ 80 – $100 h^{-1} \text{ Mpc}$ range, explaining the strong need for the nuisance parameters at the level of significance indicated by the F -test.

4.5 Significance of BAO peak detection

The $\Delta\chi^2$ curves based on fitting the mean correlation functions of the CMASS and LOWZ samples, with the ξ^{fit} and ξ^{noBAO} models are presented in Fig. 6(a). Here, the complete fitting models including the $A(s)$ fitting terms are used and $\Delta\chi^2 = \chi^2(\alpha) - \chi^2_{\text{min}}$, where χ^2_{min} is the minimum χ^2 value using the model containing BAO. A comparison of the two models shows that we detect the BAO peak in the data at an $\approx 4.3\sigma$ level for the LOWZ sample and at $\approx 8\sigma$ for the CMASS sample, in agreement with the findings of Cuesta et al. (2016). Note that we measure the BAO peak detection significance at the best-fitting value of α given by the model containing BAO. A second test of BAO significance is also captured in Fig. 6(a). For the CMASS sample, it can be seen from the plateau height of the $\Delta\chi^2$ curve (solid blue line), that local maximum lies at a value of ≈ 72 above the minimum, meaning that we can apparently be confident in our measured best-fitting value of α at $\approx 8.5\sigma$. For the LOWZ sample, the maximum lies at ≈ 20 , indicating that our best-fitting value of α is preferred at $\approx 4.0\sigma$ by the data. These values are usually taken to indicate that we have obtained well-constrained measurements of α in both cases. In the case of the LOWZ sample it can also be seen that the plateau is lower on the left-hand side ($\alpha < 0.9$) in comparison to the plateau on the right-hand side ($\alpha > 1.1$). This is once again a consequence of the flatness

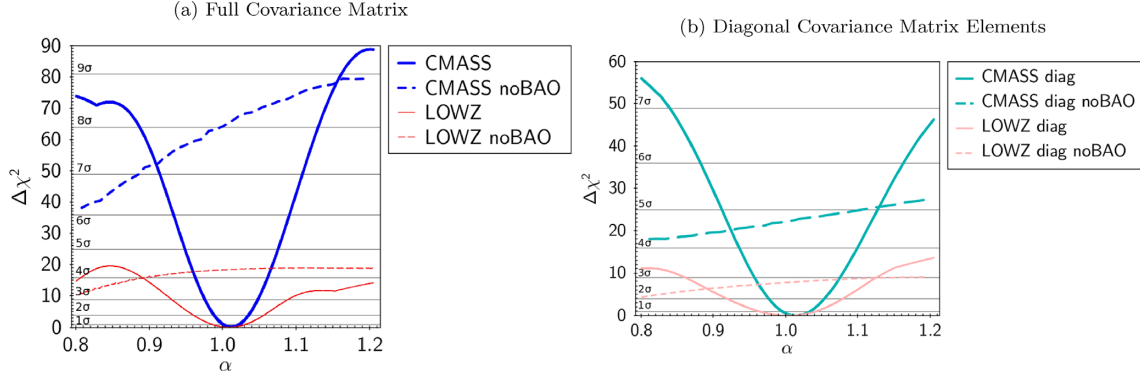


Figure 7. (a) Significance of the detection of the BAO feature based on fitting the ξ for the LOWZ (red curves) and CMASS (bold blue curves) samples in the range $28 \leq s \leq 180 h^{-1}$ Mpc. The solid lines correspond to fits to the data based on the ξ^{fit} model which contains BAO, while the dashed lines correspond to fits based on the ξ^{noBAO} model with no BAO feature. In all cases the complete models including the $A(s)$ fitting terms and the full covariance matrix are used. Here, $\Delta\chi^2 = \chi^2(\alpha) - \chi^2_{\min}$, where χ^2_{\min} is the minimum χ^2 value using the model containing BAO. Comparing the dashed and solid lines provides a measure of our level of confidence that the BAO feature exists in the data. Here, the BAO peak is detected at $\approx 4.3\sigma$ for the LOWZ sample and $\approx 8\sigma$ for the CMASS sample. (b) Same as (a) but fitting with the diagonal covariance matrix elements only.

Table 5. BAO peak detection significance using various models, along with corresponding χ^2_{\min}/dof and p -values obtained from fitting the mean correlation functions of the CMASS and LOWZ samples in the range $28 \leq s \leq 180 h^{-1}$ Mpc, using the full covariance matrix and the diagonal elements of the matrix only. As fitting with the full covariance matrix and the diagonal elements only could result in different best-fitting models, in order to ensure the fairness of the comparison, when calculating the ‘diagonal elements’ χ^2_{\min}/dof values, we use best-fitting models obtained using the full covariance matrices. Furthermore, we quote the χ^2_{\min}/dof values at fixed values of α corresponding to our measurements of the BAO peaks from Table 3 (e.g. in the case of CMASS, at 0.9892 and 0.9991 for our full and reduced models, respectively).

Sample	Model	Full matrix χ^2_{\min}/dof	p -value	Significance	Diagonal elements χ^2_{\min}/dof	p -value	Significance
CMASS	$B^2\xi_m + A(s)$	14.9/15	4.59×10^{-1}	8.0σ	2.9/15	9.99×10^{-1}	4.7σ
	$B^2\xi_m^{\text{noBAO}} + A(s)$	80.0/15	6.98×10^{-11}		25.3/15	4.61×10^{-2}	
	$B^2\xi_m$	28.5/18	5.48×10^{-2}	6.9σ	64.9/18	3.23×10^{-7}	5.8σ
	$B^2\xi_m^{\text{noBAO}}$	76.7/18	3.22×10^{-9}		98.8/18	3.67×10^{-13}	
LOWZ	$B^2\xi_m + A(s)$	15.5/15	4.16×10^{-1}	4.3σ	5.4/15	9.88×10^{-1}	2.8σ
	$B^2\xi_m^{\text{noBAO}} + A(s)$	33.9/15	3.52×10^{-3}		13.2/15	5.87×10^{-1}	
	$B^2\xi_m$	45.5/18	3.51×10^{-4}	1.8σ	47.7/18	1.67×10^{-4}	2.2σ
	$B^2\xi_m^{\text{noBAO}}$	48.8/18	1.14×10^{-4}		52.8/18	2.82×10^{-5}	

of the BAO peak in the LOWZ correlation function in the scales of $80 < s < 100 h^{-1}$ Mpc, as discussed in the previous section.

However, the level of scatter between field-to-field correlation functions around the BAO peak (as shown in Fig. 3) prompts us to caution that 8σ and 4σ BAO peak significances for CMASS and LOWZ may be overoptimistic. Although it must be remembered that these significances are calculated after the fitting of nuisance parameters which will clearly remove long-wavelength artefacts that otherwise can add to the noisy impression given by individual fields in Fig. 3.

Another consideration might also involve the anomalously low $\chi^2_{\min}/\text{dof} = 2.9/15$ recorded for our best fit to the CMASS sample with our fiducial plus nuisance parameters model, using the diagonal covariance matrix elements only, compared to 14.9/15 using the full matrix, as shown in Table 5 (with the associated $\Delta\chi^2$ plot shown in Fig. 6b). In the case of using the diagonal elements, the full noBAO model is also only rejected at $\chi^2_{\min}/\text{dof} = 25.3/15$ ($p \approx 0.046$), in comparison to the much higher rejection using the full covariance matrix $\chi^2_{\min}/\text{dof} = 80.0/15$ ($p \approx 6.98 \times 10^{-11}$).

We find similar results for the LOWZ sample with a reduction from $\chi^2_{\min}/\text{dof} = 15.5/15$ to $\chi^2_{\min}/\text{dof} = 5.4/15$ for our full model using the full and diagonal matrices, respectively. We also record a

notable reduction in the level of rejection of the noBAO model by the LOWZ data, from $\chi^2_{\min}/\text{dof} = 33.9/15$ ($p \approx 3.5 \times 10^{-3}$) using the full matrix, to a good fit with $\chi^2_{\min}/\text{dof} = 13.2/15$ ($p \approx 0.59$) using the diagonal elements.

For models with nuisance fitting parameters, using the full covariance matrix appears to increase the χ^2_{\min}/dof significantly compared to using the diagonal terms only. This is opposite to what is seen in other cases such as the fit of the fiducial ΛCDM model where no nuisance parameters are used (see Table 5). This may be due to having both positive and negative fit residuals in the first case and residuals mainly of one sign in the latter case, and a covariance matrix with exclusively positive elements. Given the size of this effect, we perform a further test by replacing the off-diagonal CMASS covariance matrix elements by zero, increasingly far from the diagonal (leaving a ‘band’ matrix). This is motivated by the correlation matrix in Fig. B1 showing that the covariance elements decrease systematically away from the diagonal. We found that $\chi^2_{\min} \approx 3$ maintained when up to the first 14 off-diagonal elements were retained and only increased to $\chi^2_{\min} \approx 15$ when elements 15–20 (indicated in Fig. B1 by the red outline) were included. This effect also appears to be important for assigning the significance of BAO peak detection (as shown in Table 5, reducing the detec-

Table 6. Results of fitting the correlation functions of the LOWZ and CMASS samples using two different models and over various fitting ranges. In performing these fits the BOSS DR12 covariance matrices were used, and as before, ‘Significance’ refers to the significance of the detection of the BAO peak using the complete fitting model.

This work	Range (h^{-1} Mpc)	Model	α	χ^2_{\min}/dof	Significance
CMASS	$28 \leq s \leq 180$	$B^2\xi_m + A(s)$	1.0109 ± 0.0121	14.9/15	8.0σ
		$B^2\xi_m$	1.0009 ± 0.0116	28.5/18	
	$36 \leq s \leq 172$	$B^2\xi_m + A(s)$	1.0134 ± 0.0117	11.9/13	6.5σ
		$B^2\xi_m$	1.0084 ± 0.0115	19.0/16	
	$44 \leq s \leq 164$	$B^2\xi_m + A(s)$	1.0153 ± 0.0119	11.0/11	6.2σ
		$B^2\xi_m$	1.0070 ± 0.0117	20.6/14	
	$52 \leq s \leq 156$	$B^2\xi_m + A(s)$	1.0143 ± 0.0125	6.6/9	6.5σ
		$B^2\xi_m$	1.0070 ± 0.0117	23.2/12	
	$60 \leq s \leq 148$	$B^2\xi_m + A(s)$	1.0133 ± 0.0123	6.3/7	7.0σ
		$B^2\xi_m$	1.0109 ± 0.0116	24.7/10	
	$68 \leq s \leq 140$	$B^2\xi_m + A(s)$	1.0148 ± 0.0118	6.2/5	7.2σ
		$B^2\xi_m$	1.0142 ± 0.0115	28.3/8	
	$76 \leq s \leq 132$	$B^2\xi_m + A(s)$	1.0114 ± 0.0129	5.6/3	5.3σ
		$B^2\xi_m$	1.0142 ± 0.0109	29.9/6	
LOWZ	$28 \leq s \leq 180$	$B^2\xi_m + A(s)$	1.0074 ± 0.0266	15.5/15	4.0σ
		$B^2\xi_m$	0.9698 ± 0.0523	45.5/18	
	$36 \leq s \leq 172$	$B^2\xi_m + A(s)$	1.0121 ± 0.0246	13.9/13	4.3σ
		$B^2\xi_m$	0.9724 ± 0.0174	49.0/16	
	$44 \leq s \leq 164$	$B^2\xi_m + A(s)$	1.0158 ± 0.0239	11.7/11	3.3σ
		$B^2\xi_m$	0.9794 ± 0.0174	48.5/14	
	$52 \leq s \leq 156$	$B^2\xi_m + A(s)$	1.0231 ± 0.0248	7.5/9	3.0σ
		$B^2\xi_m$	0.9957 ± 0.0187	39.0/12	
	$60 \leq s \leq 148$	$B^2\xi_m + A(s)$	1.0218 ± 0.0253	6.9/7	3.2σ
		$B^2\xi_m$	0.9949 ± 0.0192	43.2/10	
	$68 \leq s \leq 140$	$B^2\xi_m + A(s)$	1.0218 ± 0.0250	6.7/5	3.2σ
		$B^2\xi_m$	0.9998 ± 0.0189	42.3/8	
	$76 \leq s \leq 132$	$B^2\xi_m + A(s)$	1.0303 ± 0.0224	5.6/3	3.3σ
		$B^2\xi_m$	0.9969 ± 0.0183	31.3/6	

tion significance from 8.0σ to 4.7σ and from 4.3σ to 2.8σ for the CMASS and LOWZ when using the complete fitting model). For the CMASS sample, we observe a similar jump in the significance of peak detection from $\approx 3.5\sigma$ when only the first 13 off-diagonal elements were included, to $\approx 8\sigma$ once elements 14 and higher are included. We note that here the main contribution to the increase in $\Delta\chi^2$ (and hence the peak detection significance) appears to be from the large increase in the χ^2_{\min} of the noBAO model which rises by ~ 70 , while the χ^2_{\min} of the model containing BAO only rises by 6.5. One can similarly see this in Table 5 with the large increase of ~ 55 in the χ^2_{\min} of the noBAO+A(s) model compared to only 12 for the BAO+A(s) model, as we go from fitting with the diagonal elements only to using the full matrix. The sharp nature of this increase and its marked effect on the significance of model rejection may seem somewhat anomalous, given that one would expect relatively low correlation between $\xi(s)$ points $\approx 100 h^{-1}$ Mpc apart (as shown in Fig. B1). The sensitivity of our results to the inclusion of largely separated off-diagonal covariance matrix elements, demonstrate the importance of the accuracy of covariance matrix estimation.

4.6 The choice of fitting range

In order to investigate the effects of the choice of fitting range on our measured value of α and the significance of the detection of the BAO peak, we perform our fitting across seven different ranges using the ξ^{fit} model with and without the $A(s)$ nuisance fitting terms. We summarize the results in Table 6. It can be seen that the value of α and the magnitude of its error are largely insensitive to the choice

of the fitting range for the CMASS sample. Slight variations in the value of α are observed as the fitting range is varied in the case of the LOWZ sample, however, these values remain consistent within the uncertainties. It can be seen that the quality of the fits produced by the ξ^{fit} model without the $A(s)$ nuisance fitting terms are consistently lower than the fits produced by the complete model across various ranges as shown by the χ^2_{\min}/dof values. The quantity that appears to be most sensitive to the choice of the fitting range is the significance of the detection of the BAO peak in the data. At the two extremes, the significance of the detection of the peak varies from 8.0σ to 5.3σ for the CMASS sample and from 4.3σ to 3.0σ for the LOWZ sample, depending on the choice of the fitting range. Vargas-Magaña et al. (2016) have also examined the effect of the choice of fitting range on the robustness of the BAO peak measurement, reporting noisier results as the lower and upper bounds of the fitting range approach the BAO scale (i.e. 80 and $120 h^{-1}$ Mpc, respectively), particularly in the former case. This level of variation highlights the importance of providing appropriate justification for the choice of fitting range in studies performing analysis of the BAO feature.

4.7 Cosmological distance constraints

Using our measured values of α and 5-fields $\bar{\alpha}$ presented in Table 3 (for the complete ξ^{fit} model), and our fiducial distances presented in Table 2, we calculate the volume-averaged distance to redshift z , $D_V(z)$ for the LOWZ and CMASS samples. A comparison of our results and the findings of Cuesta et al. (2016) is given in Table 7. As expected given our measurements of α , we find our results to be

Table 7. Distance constraints obtained from the analysis of the BAO feature in the correlation function of CMASS and LOWZ samples in this work and by Cuesta et al. (2016) (Table 11). Here, $D_V(z)$ is calculated based on the value of α obtained from fitting to the mean correlation function of the samples, while the ‘5-fields $D_V(z)$ ’ values are calculated based on $\bar{\alpha}$, which is obtained by taking the mean of the values of α attained from individually fitting to the five fields in the LOWZ and CMASS samples. In both cases the α s correspond to fitting to the range $28 \leq s \leq 180 h^{-1}$ Mpc using the complete ξ^{fit} model described in equation (3). We assume a fiducial sound horizon value of $r_{d,\text{fid}} = 147.10$ Mpc. The distance constraints are quoted at the effective redshifts of $z = 0.57$ and $z = 0.32$ for the CMASS and LOWZ samples, respectively.

Study, sample	$D_V(z)r_{d,\text{fid}}/r_d$ (Mpc)	5-fields $D_V(z)r_{d,\text{fid}}/r_d$ (Mpc)
This work, CMASS	2031 ± 24	2034 ± 40
Cuesta et al. (2016), CMASS Pre-Recon	2040 ± 28	–
This work, LOWZ	1244 ± 33	1241 ± 49
Cuesta et al. (2016), LOWZ Pre-Recon	1246 ± 37	–

in agreement with those from Cuesta et al. (2016) for both samples. Furthermore, it can be seen that the magnitude of the errors are comparable between the two studies in the case of $D_V(z)$, which is based on the errors on α (giving a 2.6 and 1.2 percent distance measurement for the LOWZ and CMASS samples, respectively), while the ‘5-fields $D_V(z)$ ’ errors are larger due to the larger errors on the 5-fields $\bar{\alpha}$ values.

5 QUASAR BAO ANALYSIS

In this section, we extend our BAO analysis to higher redshifts by performing isotropic fitting to the combined monopole correlation functions of four quasar samples from the 2dF QSO Redshift Survey (2QZ; Smith et al. 2005), SDSS Data Release 5 (SDSS DR5; Adelman-McCarthy et al. 2007), 2dF-SDSS LRG and QSO survey (2SLAQ; Richards et al. 2005), and the 2dF Quasar Dark Energy Survey pilot (2QDESp; Chehade et al. 2016). In total, these surveys contain $\approx 80\,000$ quasars in the $0.3 < z < 2.2$ redshift range. As with the galaxy samples in Section 4.2, we obtain and examine the empirical error of the combined correlation function of the QSO samples, based on the scatter in the data.

In this work, we limit our samples to the range $0.8 < z < 2.2$, to allow for direct comparison and combination of our results with those from Ata et al. (2018), who performed BAO analysis on the eBOSS survey of 147 000 quasars in this redshift range. We use the published correlation function of Ata et al. (2018) and re-fit the BAO peak for α using the same techniques as for our quasar sample.

5.1 2QZ+SDSS+2SLAQ+2QDESp data sets

Here, we provide a brief summary of the relevant properties of the quasar samples used in our BAO analysis. A more detailed description of these samples can be found in the referenced papers.

The 2QZ sample (Croom et al. 2004) covers a total area of 721.6 deg^2 , containing 22 655 QSOs ($\approx 31 \text{ quasars deg}^{-2}$) up to $z \approx 3$ in the magnitude range $18.25 < b_j < 20.85$.

The SDSS DR5 ‘UNIFORM’ sample was constructed by Ross et al. (2009) by taking a subsample of the DR5 quasar catalogue (Schneider et al. 2007). This sample covers an area of $\approx 4000 \text{ deg}^2$, containing 30 239 QSOs ($\approx 8 \text{ quasars deg}^{-2}$), in the redshift range $0.3 \leq z \leq 2.2$ with a magnitude limit of $i_{\text{SDSS}} \leq 19.1$.

The 2SLAQ sample (Croom et al. 2009) covers an area of $\approx 192 \text{ deg}^2$ containing ≈ 9000 QSOs ($\approx 47 \text{ quasars deg}^{-2}$) in the redshift range $z \lesssim 3$ and magnitude range $20.5 < g_{\text{SDSS}} < 21.85$.

The 2QDESp sample (Chehade et al. 2016) covers an area of $\approx 150 \text{ deg}^2$ in the southern sky, containing $\approx 10\,000$ QSOs ($\approx 67 \text{ quasars deg}^{-2}$) with magnitudes $g \leq 22.5$. The quasars in the sample

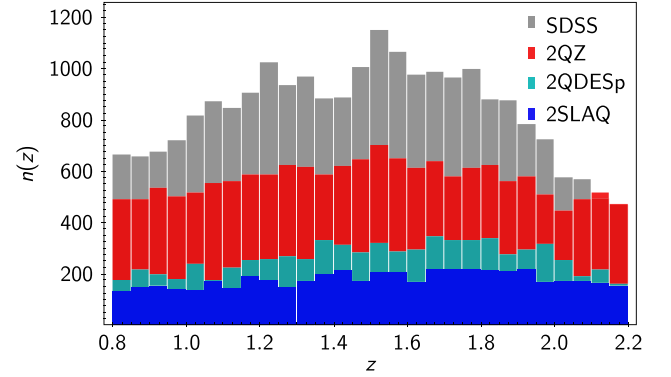


Figure 8. The redshift distribution of (from top to bottom) the SDSS DR5, 2QZ, 2QDESp and 2SLAQ QSO samples in the $0.8 < z < 2.2$ redshift range, analysed in this study.

have a mean redshift of $z = 1.55$ and with 80 per cent of the objects in the sample lying in the range $0.8 < z < 2.5$.

As mentioned above, in order to allow direct comparison and combination of our results with the measurements of Ata et al. (2018), we restrict our analysis to objects in the redshift range $0.8 < z < 2.2$. This leads to a total number of quasars N_q , of 15 926, 23 386, 4988, and 7329 for the 2QZ, SDSS, 2SLAQ, and 2QDESp samples, respectively. Fig. 8 shows the redshift distribution $n(z)$ of the four QSO samples. The weighted mean of the correlation functions of these samples is taken to represent the correlation function of the combined quasar sample (henceforth referred to as the Combined QSO sample), containing 51 629 quasars with a mean redshift of $\bar{z} = 1.5$ and an effective volume of $\approx 0.003 h^{-3} \text{ Gpc}^3$. For comparison the QSO sample of Ata et al. (2018) covers an effective volume of $\approx 0.03 h^{-3} \text{ Gpc}^3$, while the original SDSS LRG survey analysed by Eisenstein et al. (2005) covered an effective volume of $\approx 0.13 h^{-3} \text{ Gpc}^3$ and the BOSS DR12 LOWZ and CMASS samples analysed by Cuesta et al. (2016) cover effective volumes of ≈ 0.67 and $\approx 1.58 h^{-3} \text{ Gpc}^3$, respectively (in all cases we are quoting the effective volumes at $k \simeq 0.15 h \text{ Mpc}^{-1}$).

In this section, we assume the same cosmology as Ata et al. (2018) in order to facilitate direct comparison of our results, using a flat Λ CDM cosmology with $\Omega_m = 0.31$, $\Omega_b h^2 = 0.022$, $h = 0.676$. Although the mean redshift of the Combined QSO sample is $\bar{z} = 1.5$, for simplicity and ease of comparison with Ata et al. (2018), we quote our fiducial distance to $z = 1.52$ and present our D_V distance measurement at this redshift, with $D_{V,\text{fid}}(1.52) = 3871.0 \text{ Mpc}$ and $r_{d,\text{fid}} = 147.78 \text{ Mpc}$.

5.2 eBOSS

The eBOSS quasar survey is fully described by Ata et al. (2018), in which BAO measurements were performed based on a sample of 147 000 quasars in the redshift range $0.8 < z < 2.2$. With an area of $\approx 2044 \text{ deg}^2$, the quasar sky density of the sample is $\approx 72 \text{ deg}^{-2}$. Here, we simply use the correlation function from their Fig. 5 along with the QPM error bars.

6 MEASURING QSO CORRELATION FUNCTIONS

In this section, we summarize the applied methodology in our measurement of the correlation functions of the 2QDESp, 2QZ, 2SLAQ, and SDSS QSO samples. We then describe our analysis of the BAO feature in our Combined QSO sample as well as the eBOSS correlation function presented by Ata et al. (2018).

We use the Landy–Szalay estimator (described in Section 3.1), along with random catalogues generated by Chehade et al. (2016), in order to measure the correlation functions of the four QSO samples. The random catalogues are $20 \times$ larger than the data for all samples with the exception of SDSS where the random catalogue is $30 \times$ larger than the data. To account for effects of photometric and spectroscopic incompleteness, Chehade et al. (2016) have applied appropriate normalization to these randoms on a field to field basis.

All four correlation functions are calculated using twenty-five $8 h^{-1} \text{ Mpc}$ bins, following the same approach as our measurements of LOWZ and CMASS correlation functions in the previous sections. We found that the four individual correlation functions showed Poisson errors of varying sizes, where the Poisson error is given by $\sigma(s) = (1 + \xi(s))/\sqrt{DD(s)}$. The 2QZ sample has the lowest errors, with the 2SLAQ, SDSS, and 2QDESp samples having larger errors by factors of ~ 2 , ~ 1.5 , and ~ 1.5 , respectively, in our main fitting range. We therefore combined the four measured correlation functions by taking the weighted mean, given by $\hat{\xi}(s) = [\sum \xi_i(s)/\sigma_i^2(s)]/[\sum 1/\sigma_i^2(s)]$, there being little difference if we combined on the basis of summing DD , etc. pairs. We used the error on the weighted mean given by $\sigma_{\hat{\xi}(s)} = \sqrt{(\sum 1/\sigma_i^2(s))}$ as an estimate of the error. We then fit the mean correlation function for α following the procedure described in Section 3.3, in the fitting range $35 < s < 180 h^{-1} \text{ Mpc}$. This fitting range is used when reporting our main results to match the approach in Ata et al. (2018). However, we also fit the Combined QSO $\hat{\xi}(s)$ in the fitting range $35 < s < 200 h^{-1} \text{ Mpc}$ in order to study any potential effects of this choice on the results, in a similar manner as in Section 4.6.

As obtaining an accurate estimation of the covariance matrix for the Combined QSO sample requires the generation of a large set of realistic mocks, a large task which lies beyond the scope of this work, when performing the fits, we simply make use of the error on the weighted mean described above. Shanks & Boyle (1994) have shown that the relatively low space density of quasars means that at scales up to $\sim 100 h^{-1} \text{ Mpc}$, the covariance between correlation function points is low. Comparing the error on the weighted mean, to the standard error on the mean [as defined in equation (2), providing an empirical estimate of the error], we find the two measures of the uncertainty to be close in our fitting range, with the mean ratio of empirical to Poisson error being ~ 1.2 , indicating that Poisson errors are good approximations over this range. Since Poisson only applies to independent pair counts the expectation is that the covariances will be low. This view is partly supported by the measurements of Ata et al. (2018) in the eBOSS sample, who found that the correlation between adjacent points was ~ 0.2 , with the covariance

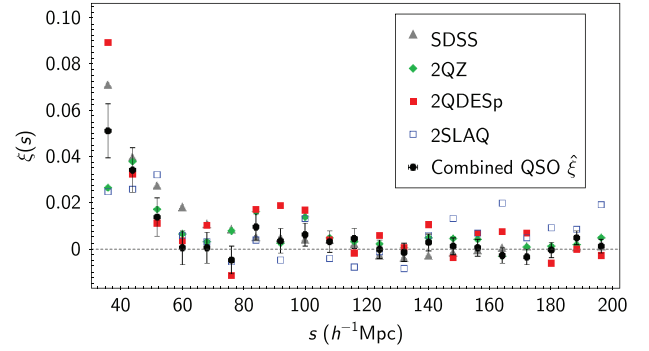


Figure 9. Correlation functions of the SDSS (grey triangles), 2QZ (green diamonds), 2QDESp (red filled squares), and 2SLAQ (blue open squares) QSO samples along with the weighted mean and the error on the weighted mean of the four samples (black). For clarity the error bars on the correlation functions of the four samples are not plotted.

matrix being dominated by the diagonal elements. Although clearly our assumption that omission of off-diagonal terms has a negligible effect in our fits needs to be further tested.

7 QSO BAO ANALYSIS: RESULTS AND DISCUSSION

In this section, we present the results of our BAO analysis in the correlation function of the Combined QSO sample as well as the eBOSS QSO correlation function of Ata et al. (2018). The correlation functions of the SDSS, 2QZ, 2QDESp, and 2SLAQ QSO samples along with the weighted mean of these correlation functions is shown in Fig. 9.

7.1 Fitting the Combined QSO sample

The results of fitting to the correlation function of the combined QSO sample with the complete ξ^{fit} model (equation 3), the ξ^{fit} model without the $A(s)$ nuisance fitting terms, and a complete ξ^{noBAO} model in the range $35 < s < 180 h^{-1} \text{ Mpc}$, are presented in Fig. 10(a). The values of α and $D_V(z)$ corresponding to the two variations of the ξ^{fit} model are presented in Table 8. In contrast to fits performed in the previous chapter, upon performing an F -ratio test it can be seen that the complete model does not provide a significantly better fit in comparison to the simple model ($F = 0.93$, $p = 0.454$). For consistency with our analysis in the previous section and that of Ata et al. (2018) however, when reporting our final results, we continue to use those corresponding to the complete model. We find that fitting the correlation function in the range $35 < s < 200 h^{-1} \text{ Mpc}$ does not have a significant effect on the measurements of the BAO peak position, resulting in a 0.8 per cent shift towards larger values of α and a 7 per cent decrease on its uncertainty.

7.2 Significance of QSO BAO peak detection

The $\Delta\chi^2$ curves from fitting the correlation function of the Combined QSO sample, with the ξ^{fit} and ξ^{noBAO} models in our two different fitting ranges are presented in Fig. 11. A comparison of the curves shows that in the $35 < s < 180 h^{-1} \text{ Mpc}$ range, the BAO peak is detected at $\approx 1.4\sigma$ in the data, while in the $35 < s < 200 h^{-1} \text{ Mpc}$ range, the peak is detected at a higher significance of $\approx 1.9\sigma$. This is in line with our finding in Section 4.6

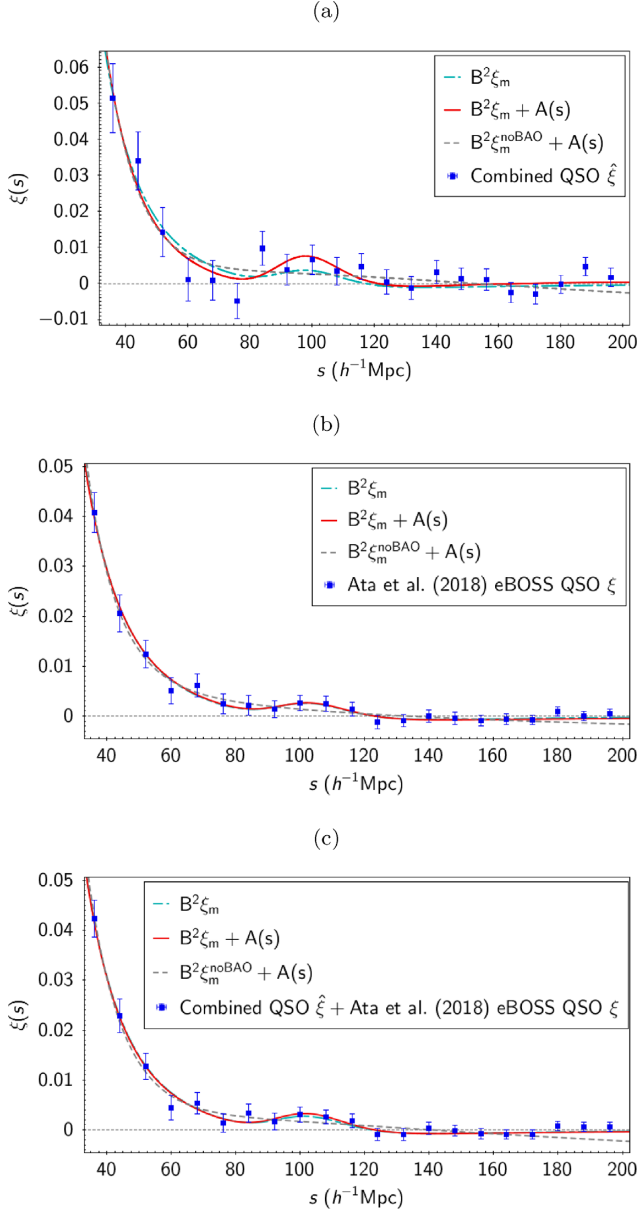


Figure 10. (a) The results of fitting the weighted mean of the 2QZ, SDSS, 2SLAQ, and 2QDESp quasar samples' correlation functions. The error bars are the error on the weighted mean. The fitting is performed using various models for bins in the range $35 < s < 180 \ h^{-1} \text{Mpc}$. The dot-dashed light blue curve is the ξ^{fit} model (equation (3)) with the B fitting parameter only, while the solid red curve shows the complete ξ^{fit} model. The dashed grey curve is the ξ^{noBAO} model fitted with the B and $A(s)$ fitting terms. (b) The eBOSS QSO correlation function taken from fig. 5 of Ata et al. (2018) along with the QPM error bars. Also shown is our three fits to the correlation function using the same models as in subplot (a). Note that the fit given by the $B^2\xi(s)$ model (dot-dashed light blue curve) is in this case very similar to that given by our complete fitting model (solid red curve) and is therefore covered by complete model in this plot. This is also reflected in table 5 of Ata et al. (2018), with the fits using two models producing very similar results. (c) The weighted mean of our Combined QSO correlation function (subplot a) and the eBOSS QSO correlation function (subplot b). Fits using our three models are shown with the correlation function clearly being dominated by the eBOSS data due to its smaller error bars.

where we demonstrated that the choice of the fitting range can have a large effect on the significance of detection of the BAO peak.

7.3 BAO fits to eBOSS quasar correlation function

In this section, we perform a test of our BAO analysis techniques by fitting to the eBOSS QSO correlation function of Ata et al. (2018). Fig. 10(b) shows the eBOSS quasar DR14 correlation function of Ata et al. (2018) taken from their fig. 5. We use the estimate with systematic weights applied (their solid line). The points are plotted in our Fig. 10(b) as $\xi(s)$ rather than $s^2\xi(s)$ for consistency with our LRG fits. We fit these data using the same nuisance parameters as previously and, as in Section 7.1, we neglect the off-diagonal terms of the covariance matrix on the grounds that Ata et al. (2018) report low covariance between $\xi(s)$ points (< 0.2). Table 8 shows the results. We find $\alpha = 1.012 \pm 0.051$ compared to their $\alpha = 0.996 \pm 0.039$. Thus, the estimates of α are similar but we report an ≈ 35 per cent larger error. Our $\chi^2/\text{dof} = 3.0/13$ is small compared to their $\chi^2/\text{dof} = 8.6/13$. Comparison against the best-fitting noBAO model (grey curve in our Fig. 10b) shows only a 1.4σ detection of the BAO peak compared to 2.8σ obtained by Ata et al. (2018). Again based on our findings in Section 4.5, this lower significance of detection is likely due to the fact that we are only using the error bars of Ata et al. (2018) (the square root of the diagonal elements of their covariance matrix) to perform the fitting. If so, the same behaviour as discussed in Section 4.5 is hinted at here. However, as the covariance matrix of Ata et al. (2018) is currently not available to us, we are unable to draw a comparison between this measurement and the peak detection significance obtained using the full matrix in a similar manner to Section 4.5.

With the eBOSS correlation function errors ≈ 40 per cent the size of those of the Combined QSO correlation function in Fig. 10(a), the eBOSS result is expected to dominate the combination of these two. This is confirmed by our fits to the weighted mean of the two correlation functions shown in Fig. 10(c), and by the value of $\alpha = 1.003 \pm 0.044$ with a significance of peak detection against the best-fitting noBAO model of 1.5σ shown in Table 8.

We find the errors on the correlation function of our Combined QSO sample to be $\sim 2.5 \times$ larger than those of eBOSS, and similarly, the error on α was $\sim 2 \times$ larger (7.6 per cent versus 3.9 per cent). This is roughly in line with the expectation as the eBOSS sample has an $\sim 10 \times$ larger effective volume, with errors scaling as $V_{\text{eff}}^{-1/2}$. However, we find the same 1.4σ BAO peak detection significance in our fits to the eBOSS sample and our Combined QSO sample. This is probably due to the fitted amplitude (B^2) for our QSO sample being unexpectedly $\sim 2 \times$ larger than for eBOSS, and emphasising that BAO scales can appear relatively well measured (~ 7.6 per cent) in samples where the peak is barely detectable above noise. With this caveat, if we then weigh by the respective errors on α as measured by us for our combined sample and by the error of Ata et al. (2018) for eBOSS, the result is $\alpha = 1.005 \pm 0.035$.

7.4 BAO distance constraints on $D_V(z)$

We present our measured value of D_V based on our fit to the weighted mean of our Combined QSO sample and the eBOSS correlation function of (Ata et al. 2018, ; Table 8), as well as our D_V measurements for the BOSS DR12 CMASS and LOWZ samples (presented in Table 7 of Section 4.7), in Fig. 12. The pre-reconstruction measurements of D_V by Cuesta et al. (2016) based on the DR12 CMASS and LOWZ samples, as well as those from Beutler et al. (2011) for the 6dFGS sample, Ross et al. (2015) for the SDSS DR7 Main

Table 8. (I) Results of fitting the correlation functions of the Combined QSO sample using the complete ξ^{fit} model described in equation (3) and the same model without the $A(s)$ nuisance fitting parameters, in the range $35 < z < 180 h^{-1}\text{Mpc}$. (II) The eBOSS QSO BAO measurements presented by Ata et al. (2018). (III) Our BAO measurements based on fitting the eBOSS QSO correlation function presented in fig. 5 of Ata et al. (2018) along with their QPM errors. (IV) Results of our fit to the weighted mean of the combined QSO and eBOSS correlation functions. The distance constraint on D_V calculated based on the measured values of α are included for each case. Based on our fiducial cosmology, we assume a fiducial sound horizon value of $r_{d,\text{fid}} = 147.78 \text{ Mpc}$. Here, the value of $D_V(z)$ is quoted at $z = 1.52$.

Data set	Model	α	$\chi^2_{\text{min}}/\text{dof}$	Significance	$D_V(z)r_{d,\text{fid}}/r_d \text{ (Mpc)}$
(I) Combined QSO	$B^2\xi_m + A(s)$	1.042 ± 0.079	11.6/13	1.4σ	4034 ± 306
	$B^2\xi_m$	1.033 ± 0.106	14.1/16	1.8σ	3999 ± 410
(II) eBOSS QSO	$B^2\xi_m + A(s)$	0.996 ± 0.039	8.6/13	2.8σ	3856 ± 151
(III) Our fit to eBOSS QSO	$B^2\xi_m + A(s)$	0.988 ± 0.050	3.0/13	1.4σ	3825 ± 194
(IV) Combined QSO+eBOSS	$B^2\xi_m + A(s)$	0.997 ± 0.042	5.5/13	1.5σ	3859 ± 163

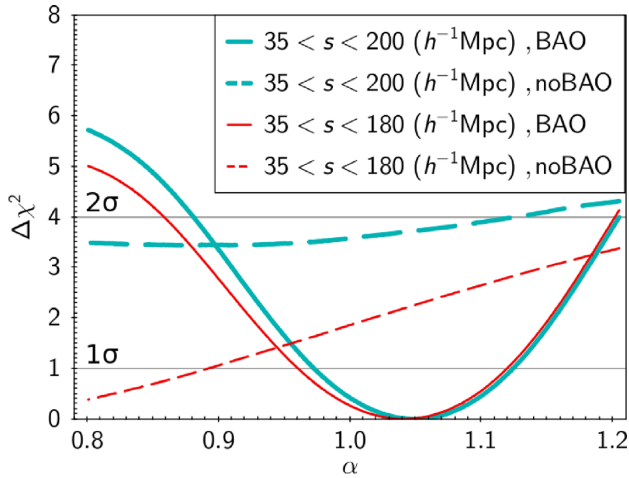


Figure 11. The significance of the detection of the BAO peak based on fitting to the correlation function of the Combined QSO sample in the range $35 < s < 180 h^{-1} \text{ Mpc}$ (red curves) and $35 < s < 200 h^{-1} \text{ Mpc}$ (bold blue curves). The solid curves correspond to a fits to the data based on the ξ^{fit} model which contains BAO, while the dashed curves correspond to the fits based on the ξ^{noBAO} model with the BAO feature removed. In both cases the complete models including the $A(s)$ fitting terms are used. Here, $\Delta\chi^2 = \chi^2(\alpha) - \chi^2_{\text{min}}$, where χ^2_{min} is the minimum χ^2 value using the model containing BAO. Comparing the two curves indicates that the BAO peak is detected at an $\approx 1.4\sigma$ and $\approx 1.9\sigma$ level in the $35 < s < 180$ and $35 < s < 200 h^{-1} \text{ Mpc}$ ranges, respectively.

sample and Kazin et al. (2014) for the WiggleZ galaxy sample are also included for comparison. The flat ΛCDM prediction based on the Planck 2016 cosmology (TT, TE, EE+lowP+lensing+ext parameters from table 4 of Planck Collaboration 2016) is added for comparison. The grey region represents the 1σ variation on the Planck prediction of $D_V(z)$. As these variations are dominated by the uncertainties in $\Omega_m h^2$ (see e.g. Anderson et al. 2014), this region is determined via sampling $\Omega_m h^2$ under the assumption that it follows a Gaussian distribution given by the Planck 2016 measurement and its 68 per cent confidence limit.

For the LOWZ, CMASS, and Combined QSO + eBOSS samples, we find a good agreement between our measurement of D_V and the Planck 2016 prediction. As shown by the $\chi^2_{\text{min}}/\text{dof}$ values in Table 9, regardless of using our measurements of D_V for the LOWZ and CMASS samples or those of Cuesta et al. (2016), overall the ΛCDM model provides a reasonably good fit to the data. Although the results appear to be overfitted.

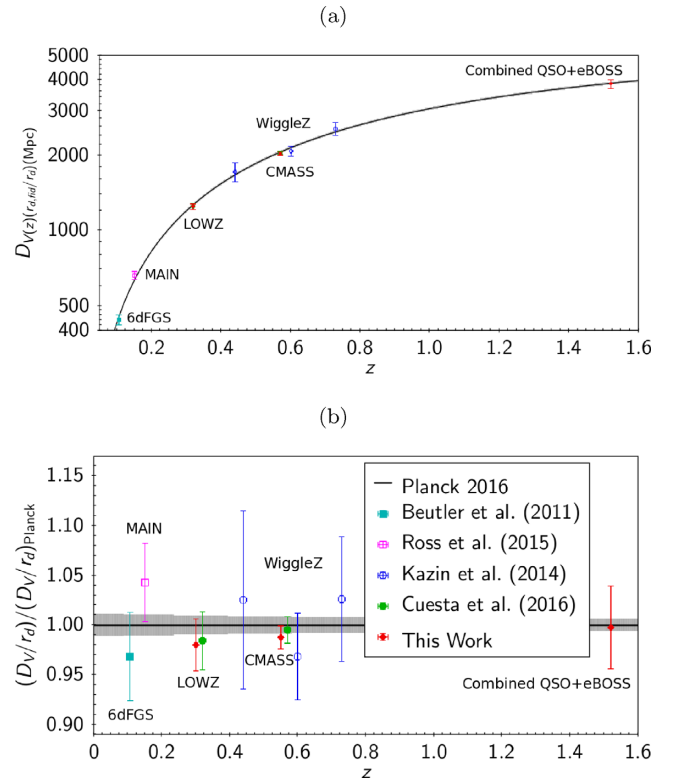


Figure 12. A comparison of our measured values of D_V for the LOWZ, CMASS and Combined QSO+eBOSS samples (filled red diamonds) with the predictions based on a flat ΛCDM model with the Planck 2016 parameters (solid black line). The grey region represents the 1σ variation on the Planck prediction of $D_V(z)$. The measurements of D_V from Cuesta et al. (2016) for the CMASS and LOWZ samples (filled green circles), Beutler et al. (2011) for the 6dFGS sample (filled light blue square), Ross et al. (2015) for the SDSS DR7 Main sample (open pink square) and Kazin et al. (2014) for the WiggleZ galaxy sample (open dark blue circles), are also included for comparison. For easier comparison, in subplot (b) we have normalized the results to Planck 2016 and shifted our measurements for the LOWZ and CMASS samples along the x-axis.

8 CONCLUSIONS

In this study, we first obtained an independent empirical estimate of errors on the correlation functions of the BOSS DR12 LOWZ and CMASS samples. This was done by dividing each sample into subsamples, measuring the correlation functions for these fields individually and taking standard and bootstrap errors around the mean

Table 9. Results of fitting the Λ CDM model to the $D_V(z)(r_{d, fid}/r_d)$ values plotted in Fig. 12. As there are two sets of measurements for LOWZ and CMASS, we fit to two subsets of the data with (i) our measurements, (ii) (Cuesta et al. 2016) measurements.

Subset	Λ CDM+Planck (2015)	
	χ^2_{\min}/dof	p -value
(i)	4.1/7	0.77
(ii)	2.9/7	0.89

to represent the correlation function error of the entire sample. For both samples, we found general agreement between these empirical errors and those measured by Cuesta et al. (2016) from 1000 simulated DR12 QPM mocks.

Using the DR12 QPM covariance matrix of Cuesta et al. (2016), we have obtained measurements of the position of the BAO peak based on isotropic fits, both to our mean correlation functions and to the correlation functions of 5 subsamples and taking the mean of the results. Using either method, we found our results to be in agreement with those from Cuesta et al. (2016) for both samples. Similarly, our measurement of the volume averaged distance $D_V(z)$ for both samples is in agreement with the result from Cuesta et al. (2016) and the predictions from Planck Collaboration (2016).

We have demonstrated that the $A(s)$ nuisance fitting parameters play a significant role in producing a good fit, when fitting the correlation functions with a fiducial Λ CDM model. At our primary fitting range, an F -ratio test shows that the simple Λ CDM model without the $A(s)$ nuisance parameters is a significantly worse fit to the data compared to the full model, especially in the case of the LOWZ sample where the shape of the BAO peak appears flat to one side.

By testing the effect of the choice of fitting range on our measurements we have further demonstrated that the measured position of the BAO peak and its uncertainty are largely insensitive to the choice of fitting range. However, the estimated significance of peak detection varies considerably depending on this choice by up to 30 per cent for both CMASS and LOWZ samples.

Interestingly, we observed a significant reduction in the χ^2_{\min}/dof values when fitting the CMASS and LOWZ correlation functions using only the diagonal elements of the BOSS DR12 QPM covariance matrix. We mainly observed this effect in our fits where we included the nuisance parameters in the model. In these cases, the reduction in χ^2_{\min}/dof values resulted in notably lower rejections of our noBAO model as well as a reduction in the BAO peak detection significances (from 8.0σ to 4.7σ for CMASS, and from 4.3σ to 2.8σ for LOWZ). This result shows how important the accuracy of the covariance matrix is to the determination of BAO peak significance, even at large $\approx 100 h^{-1}$ Mpc separations between $\xi(s)$ points.

In Section 5, we extended our analysis to higher redshifts by performing fitting to the weighted mean of the correlation functions of the 2QZ, SDSS DR5, 2SLAQ, and 2QDES quasar samples. Here, the BAO feature was detected at $\approx 1.4\sigma$ in the data. Fitting the correlation function of our Combined QSO sample resulted in a distance constraint of $D_V(z = 1.52)r_{d, fid}/r_d = 4034 \pm 306$ Mpc (assuming $r_{d, fid} = 147.78$ Mpc), a 7.6 per cent measurement to $z = 1.52$. This value is in agreement with the prediction from Planck Collaboration (2016), as well as the eBOSS 3.9 per cent measurement of $D_V(z = 1.52)r_{d, fid}/r_d = 3856 \pm 151$ Mpc. The main possible disagreement with the eBOSS analysis again lies in the question of the BAO peak significance since, using effectively only the diagonal

elements of their covariance matrix in our fit to the eBOSS correlation function, we found a 1.4σ result (with $\chi^2_{\min}/\text{dof} = 3.0/13$), compared to their 2.8σ result (with $\chi^2_{\min}/\text{dof} = 8.6/13$), obtained using the full matrix.

Whether we use our BAO peak results for CMASS and LOWZ or those of Cuesta et al. (2016), there appears to be no disagreement with the standard Planck prediction for the $D_V(z)$ diagram. So once the peaks are identified, there seems little difference in the measured values of the peak positions or broadly in the errors on these positions. The main potential issue appears to be in the detection significance of the peaks which may be up to $1.7 \times$ smaller than claimed in the case of CMASS LRGs and $2 \times$ smaller for eBOSS quasars if only diagonal covariance matrix elements are used. Clearly our results emphasise the importance of accurate covariance matrices in correlation function analysis, even at the largest $\approx 100 h^{-1}$ Mpc ‘lags’ between $\xi(s)$ points. In the case of CMASS LRGs, even using our lower (4.7σ) estimate of BAO detection significance means that there is no doubt of a clear BAO detection, even before reconstruction. But for quasar samples, our lower (1.4σ) detection significance estimates mean that more data may be required to establish that the BAO peak has been unambiguously detected. It will be interesting to confirm the current quasar BAO peak detections with the full eBOSS sample and then future quasar samples from e.g. DESI.

ACKNOWLEDGEMENTS

We would like to thank Ben Chehade, Ruari Mackenzie, and Paddy Alton for their valuable advice and discussions. Additional thanks goes to Antonio J. Cuesta for kindly providing the measured correlation functions as well as the BOSS DR12 covariance matrices used in the analysis of Cuesta et al. (2016). We would also like to thank David Alonso for providing public access to the CUTE code used in obtaining the correlation functions in this study. We would also like to thank the anonymous referee for their thorough review of this work and their helpful comments and suggestions.

Funding for SDSS-III has been provided by the Alfred P. Sloan Foundation, the Participating Institutions, the National Science Foundation, and the U.S. Department of Energy Office of Science. The SDSS-III web site is <http://www.sdss3.org/>.

Funding for the Sloan Digital Sky Survey IV has been provided by the Alfred P. Sloan Foundation, the U.S. Department of Energy Office of Science, and the Participating Institutions. SDSS acknowledges support and resources from the Center for High-Performance Computing at the University of Utah. The SDSS web site is www.sdss.org.

SDSS is managed by the Astrophysical Research Consortium for the Participating Institutions of the SDSS Collaboration including the Brazilian Participation Group, the Carnegie Institution for Science, Carnegie Mellon University, the Chilean Participation Group, the French Participation Group, Harvard-Smithsonian Center for Astrophysics, Instituto de Astrofísica de Canarias, The Johns Hopkins University, Kavli Institute for the Physics and Mathematics of the Universe (IPMU)/University of Tokyo, Lawrence Berkeley National Laboratory, Leibniz Institut für Astrophysik Potsdam (AIP), Max-Planck-Institut für Astronomie (MPIA Heidelberg), Max-Planck-Institut für Astrophysik (MPA Garching), Max-Planck-Institut für Extraterrestrische Physik (MPE), National Astronomical Observatories of China, New Mexico State University, New York University, University of Notre Dame, Observatório Nacional/MCTI, The Ohio State University, Pennsylvania State University, Shanghai Astronomical Observatory, United Kingdom Participation Group, Universidad Nacional

Autónoma de México, University of Arizona, University of Colorado Boulder, University of Oxford, University of Portsmouth, University of Utah, University of Virginia, University of Washington, University of Wisconsin, Vanderbilt University, and Yale University.

REFERENCES

- Adelman-McCarthy J. K. et al., 2007, *ApJS*, 172, 634
 Alam S. et al., 2015, *ApJS*, 219, 12
 Alonso D., 2012, preprint (arXiv:1210.1833)
 Anderson L. et al., 2012, *MNRAS*, 427, 3435
 Anderson L. et al., 2014, *MNRAS*, 441, 24
 Ata M. et al., 2018, *MNRAS*, 473, 4773
 Ballinger W. E., Peacock J. A., Heavens A. F., 1996, *MNRAS*, 282, 877
 Beutler F. et al., 2011, *MNRAS*, 416, 3017
 Blake C., Glazebrook K., 2003, *ApJ*, 594, 665
 Chehade B. et al., 2016, *MNRAS*, 459, 1179
 Croom S. M., Smith R. J., Boyle B. J., Shanks T., Miller L., Outram P. J., Loaring N. S., 2004, *MNRAS*, 349, 1397
 Croom S. M. et al., 2009, *MNRAS*, 392, 19
 Cuesta A. J. et al., 2016, *MNRAS*, 457, 1770
 Dawson K. S. et al., 2016, *AJ*, 151, 44
 Delubac T. et al., 2015, *A&A*, 574, A59
 Dolney D., Jain B., Takada M., 2006, *MNRAS*, 366, 884
 Eisenstein D. J., Hu W., 1998, *ApJ*, 496, 605
 Eisenstein D. J. et al., 2005, *ApJ*, 633, 560
 Feldman H. A., Kaiser N., Peacock J. A., 1994, *ApJ*, 426, 23
 Glazebrook K., Blake C., 2005, *ApJ*, 631, 1
 Gregory P., 2005, *Bayesian Logical Data Analysis for the Physical Sciences*. Cambridge Univ. Press, New York, NY
 Kazin E. A. et al., 2014, *MNRAS*, 441, 3524
 Landy S. D., Szalay A. S., 1993, *ApJ*, 412, 64
 Lewis A., Challinor A., Lasenby A., 2000, *ApJ*, 538, 473
 Linder E. V., 2003, *Phys. Rev. D*, 68, 083504
 Matsubara T., 2004, *Astrophys. J.*, 615, 573
 Norberg P., Baugh C. M., Gaztañaga E., Croton D. J., 2009, *MNRAS*, 396, 19
 Peebles P. J. E., 1980, *The Large-Scale Structure of the Universe*. Princeton Univ. Press, Princeton, NJ
 Peebles P. J., Ratra B., 2003, *Rev. Mod. Phys.*, 75, 559
 Perlmutter S. et al., 1999, *ApJ*, 517, 565
 Planck Collaboration, 2016, Planck 2015 results. XIII. Cosmological parameters, *A&A*, 594, A13
 Reid B. et al., 2016, *MNRAS*, 455, 1553
 Richards G. T. et al., 2005, *MNRAS*, 360, 839
 Riess A. G. et al., 1998, *AJ*, 116, 1009
 Ross N. P. et al., 2009, *ApJ*, 697, 1634
 Ross A. J., Samushia L., Howlett C., Percival W. J., Burden A., Manera M., 2015, *MNRAS*, 449, 835
 Ross A. J. et al., 2017, *MNRAS*, 464, 1168
 Sánchez A. G., Baugh C. M., Angulo R. E., 2008, *MNRAS*, 390, 1470
 Sawangwit U., Shanks T., Croom S. M., Drinkwater M. J., Fine S., Parkinson D., Ross N. P., 2012, *MNRAS*, 420, 1916
 Schneider D. P. et al., 2007, *AJ*, 134, 102
 Seo H.-J., Eisenstein D. J., 2003, *ApJ*, 598, 720
 Shanks T., 1985, *Vistas Astron.*, 28, 595
 Shanks T., Boyle B. J., 1994, *MNRAS*, 271, 753
 Slosar A. et al., 2013, *J. Cosmol. Astropart. Phys.*, 4, 026
 Smith R. J., Croom S. M., Boyle B. J., Shanks T., Miller L., Loaring N. S., 2005, *MNRAS*, 359, 57
 Squires G. L., 2001, *Practical Physics*, 4th edn. Cambridge Univ. Press, Cambridge
 Vargas-Magaña M. et al., 2016, preprint (arXiv:1610.03506)
 White M., Tinker J. L., McBride C. K., 2014, *MNRAS*, 437, 2594
 Xu X., Padmanabhan N., Eisenstein D. J., Mehta K. T., Cuesta A. J., 2012, *MNRAS*, 427, 2146

APPENDIX A: CMASS 30 FIELDS

Here, we present a brief comparison of the errors achieved using the original five subsamples and an increased number of subsamples (30) to test the robustness of our estimated errors to subsample size. The position of the 30 selected fields are shown in Fig. A1 and the corresponding correlation functions in Fig. A2. Each field contains about 23 500 galaxies and has an area of $\simeq 275 \text{ deg}^2$, with the selected fields covering 88 percent of the total sample area. We find the mean correlation function to be in a good agreement with the mean correlation function from our five fields as well as the CMASS correlation function from Cuesta et al. (2016), once integral constraint (as discussed in Peebles 1980) is accounted for. We estimate the bootstrap error on the CMASS correlation function

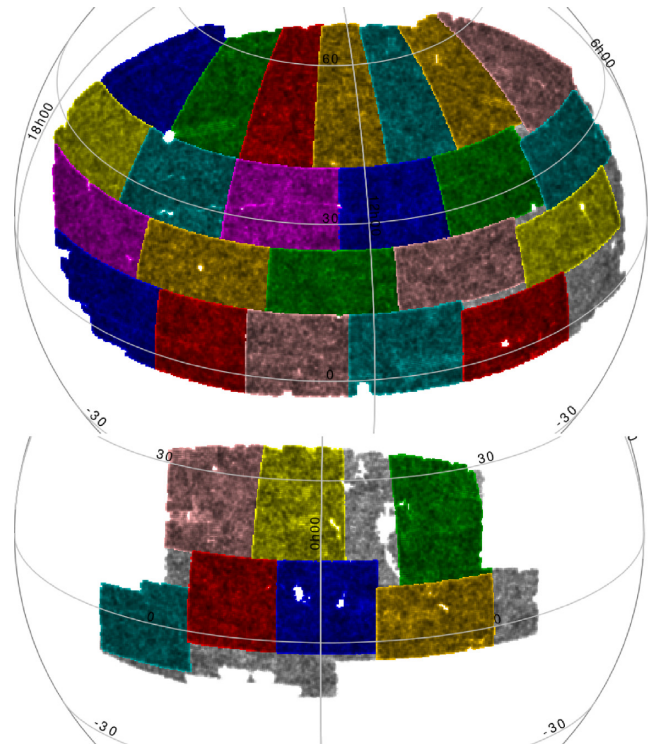


Figure A1. The coverage of the chosen 30 fields in the Northern (top) and Southern (bottom) Galactic caps of the CMASS sample. The selected fields are highlighted by various colours while the unselected areas are shown in grey. These subsamples are used in order to obtain a more accurate bootstrap estimation of the correlation function errors from the data.

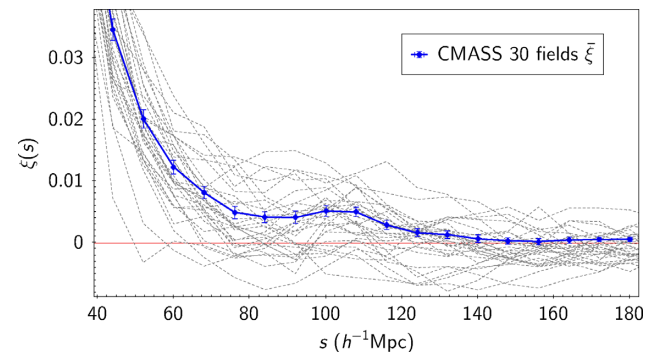


Figure A2. Correlation functions of the 30 fields in the CMASS sample (grey dashed lines) and the mean correlation function (solid blue line). The error bars on the mean correlation function are the standard error on the mean.

based on these 30 subsamples and compare the results with our errors based on the original five subsamples in Fig. 5(a).

APPENDIX B: CMASS CORRELATION MATRIX

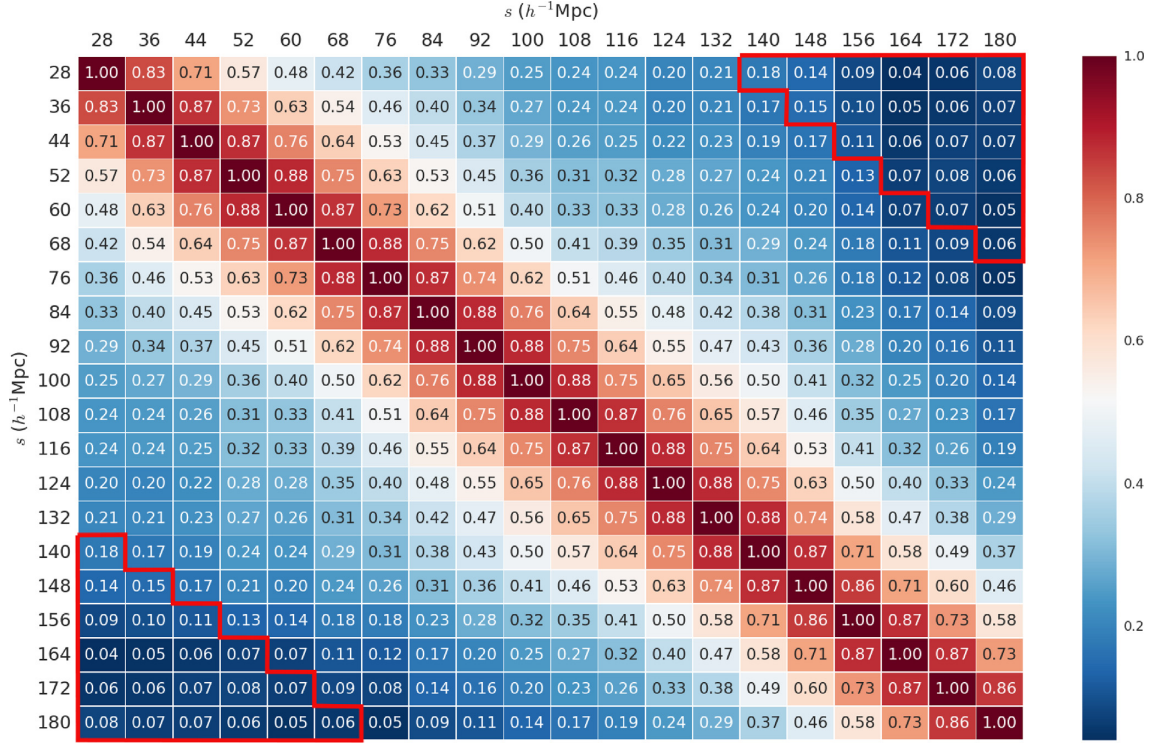


Figure B1. CMASS DR12 correlation matrix based on the covariance matrix used in the analysis of Cuesta et al. (2016), as well as in our fits in this work. The red outlines indicates the 15–20 off-diagonal elements corresponding to covariance matrix terms which appear to be essential in obtaining a reasonable $\chi^2_{\min} \approx 15$, as shown in our test in Section 4.5.

This paper has been typeset from a \LaTeX file prepared by the author.